Anal Bioanal Chem (2017) 409:5855–5874
DOI 10.1007/s00216-017-0499-z

REVIEW

Perspectives and challenges of photon-upconversion nanoparticles - Part I: routes to brighter particles and quantitative spectroscopic studies

Ute Resch-Genger[1] · **Hans H. Gorris**[2]

Received: 30 March 2017 / Revised: 29 May 2017 / Accepted: 27 June 2017 / Published online: 14 July 2017

Abstract Lanthanide-doped photon-upconversion nanoparticles (UCNPs) have been the focus of many research activities in materials and life sciences in the last 15 years because of their potential to convert light between different spectral regions and their unique photophysical properties. To fully exploit the application potential of these fascinating nanomaterials, a number of challenges have to be overcome, such as the low brightness, particularly of small UCNPs, and the reliable quantification of the excitation-power-density-dependent upconversion luminescence. In this series of critical reviews, recent developments in the design, synthesis, optical-spectroscopic characterization, and application of UCNPs are presented with special focus on bioanalysis and the life sciences. Here we guide the reader from the synthesis of UCNPs to different concepts to enhance their luminescence, including the required optical-spectroscopic assessment to quantify material performance; surface modification strategies and bioanalytical applications as well as selected examples of the use of UCNPs as reporters in different assay formats are addressed in part II. Future trends and challenges in the field of upconversion are discussed with special emphasis on UCNP synthesis and material characterization, particularly quantitative luminescence studies.

Keywords Photon upconversion · Lanthanides · Nanomaterials · Fluorescence · Quantification · Background-free imaging · Dye sensitization · Förster resonance energy transfer · Plasmonics

✉ Ute Resch-Genger
ute.resch@bam.de

[1] Federal Institute for Materials Research and Testing (BAM), Richard-Willstaetter-Str. 11, 12489 Berlin, Germany

[2] Institute of Analytical Chemistry, Chemo- and Biosensors, University of Regensburg, 93040 Regensburg, Germany

Introduction

The process of upconversion (UC) luminescence (UCL) comprises excitation of a solid-state material or molecular system with lower-energy photons that stimulates the emission of higher-energy photons (anti-Stokes-shifted luminescence) via real intermediate excited electronic states. This distinguishes it from other optical processes that also rely on multiphoton absorption, such as multiphoton (commonly two-photon) fluorescence and second (third, fourth, etc.) harmonic generation, that involve virtual electronic states and hence require much higher excitation power densities (*P*). UC processes are typically divided into lanthanide (Ln^{3+})-based UC using emissive Ln^{3+} ions, although transition metal and actinide ions are also capable of UC, and triplet–triplet annihilation based UC, which typically utilizes the matching triplet states of two different dye molecules as intermediate excited states [1, 2] and is beyond the scope of this review. Most Ln^{3+}-based UC materials rely on a solid inorganic matrix such as a glass or a crystalline host such as a metal fluoride (e.g., $NaYF_4$, CaF_2), oxide (Y_2O_3), phosphate (YPO_4), or vanadate ($GdVO_4$) doped with a single Ln^{3+} ion or a combination of Ln^{3+} ions such as Er^{3+}, Yb^{3+}, Tm^{3+}, Ho^{3+}, Nd^{3+}, and Gd^{3+} [3]. UC processes in bulk materials such as glasses and micrometer- and submicrometer-sized phosphors, which involve multiple electronic transitions of the absorbing and emitting Ln^{3+} ions influenced by ion–lattice interactions, have been studied for decades. In the last decade, Ln^{3+}-doped photon-UC nanoparticles (UCNPs) [4–13] have emerged particularly as a new class of nanocrystalline luminescent reporters for the life and material sciences. The UCL dynamics

in these UCNPs, which are the focus of this review, are more complicated because of variations in both the chemical structure and the electronic structure and particularly surface effects. In addition, also a very small, yet increasing number of molecular Ln^{3+}-based UC systems have been reported. Examples include an ion-associated complex of an Er^{3+} chelate of 2-thenoyltrifluoroacetone and a near-infrared (NIR)-emissive cyanine dye [14], a macrocyclic erbium complex bridged by fluoride anions [15], Yb^{3+}-based supramolecular heteropolynuclear complexes [16], and polynuclear chromium(III)–lanthanide (e.g., Yb^{3+}) complexes [17].

Recent progress in the synthesis and surface modification of UCNPs and a better mechanistic understanding of the underlying photophysics have provided the ground for an ever-increasing number of (bio)analytical, diagnostic, and sensing applications as well as photovoltaic and security applications. A hallmark of UCNPs among the different classes of luminescent materials listed in Table 1 is their unique property of emitting shorter-wavelength light on NIR excitation [anti-Stokes emission; NIR-to-ultraviolet (UV)/visible/NIR conversion]. On NIR excitation, conventional organic fluorophores are not excited, and light scattering is minimal such that UCNPs can be detected without optical background interference.

The potential of UCNPs cannot be fully appreciated without an understanding of their photophysical features. Most UCNPs consist of a nanocrystalline fluoride or oxide host matrix such as $NaYF_4$ or Gd_2O_3 doped with a single Ln^{3+} ion or several Ln^{3+} ions. The arrangement of electrons within the $4f^n$ configuration of the dopant lanthanides is substantially diverse, resulting in a large number of energy levels and hence a manifold of emission bands and colors [18, 19]. In co-doped UCNPs, one type of Ln^{3+} dopant serves as a sensitizer ion that absorbs NIR light and—after multiple energy transfer steps between neighboring sensitizer ions—transfers the excitation energy to a neighboring activator ion in sequential steps (energy transfer UC). Energy transfer can be controlled by parameters such as the combination of dopants and interion distance d [energy transfer efficiency is proportional to d^{-6} for dipole–dipole energy transfer and is proportional to $\exp(-d/d_0)$ for exchange coupling], and thus by dopant concentration and spacing in the respective crystal lattice or core–shell particle architecture, as well as by tuning of the population of the energy levels of the sensitizer/donor and activator/acceptor

Table 1 Summary of the spectroscopic features of photon-upconversion nanoparticles (*UCNPs*) principally advantageous for bioanalytical applications compared with other commonly used classes of emitters such as organic dyes and semiconductor nanocrystals (quantum dots)

Features of UCNPs	Unlike	Advantages and applications
NIR light excitation (commonly 980 nm)	Fluorescent dyes/conventional II/VI quantum dots	Background-free diagnostic assays. Particularly well suited for deep tissue/small animal imaging
Long-lived intermediate energy levels	Fluorescent dyes/quantum dots	Sequential absorption of two or more NIR photons. Excitation with comparably low energy and inexpensive CW-light sources. Typically very low background noise
Anti-Stokes-shifted emission	Fluorescent dyes/quantum dots	Conversion of light between different spectral regions, i.e., NIR-to-UV/vis/(shorter) NIR. No spectral cross talk, excellent separation of excitation and detection wavelengths/spectral windows
Narrow and multiple emission bands in the UV, vis, and NIR regions	Fluorescent dyes (except for dual emissive dyes)/quantum dots	Spectral multiplexing and ratiometric measurements. A possible drawback excitation is of autofluorescence by UCL
Long (and partly tunable) luminescence lifetimes (microsecond range)	Fluorescent dyes/quantum dots (except for doped quantum dots)	Time-gated emission measurements. Lifetime multiplexing. Use as donors in time-resolved Förster resonance energy transfer detection schemes. A possible drawback is the reduced number of emitted photons per time interval (slow photocycle) and hence elongated measurement times
No photobleaching or photobrightening	Fluorescent dyes/quantum dots	Long-term imaging
No blinking	Fluorescent dyes/quantum dots	Single-particle applications
Magnetic (e.g., co-dopant Gd^{3+})	Fluorescent dyes	Dual imaging such as combined optical and magnetic resonance imaging
Low toxicity	Quantum dots	Cell imaging and bioimaging
Narrow emission bands also in the SWIR (e.g., downshifted emission)	Fluorescent dyes	NIR-to-SWIR light conversion. Optical reporters for bioimaging in the SWIR (approximately 1000 to 1700 nm)

The properties and limitations of UCNPs are discussed in the text.

CW continuous wave, *NIR* near infrared, *SWIR* short wavelength infrared (here used for the spectral region from approximately 1000 to 1700 nm), *UCL* upconversion luminescence, *UV* ultraviolet, *vis* visible

ions, and hence P [20]. Energy can be transferred between dopants also via the reverse process of cross relaxation (CR), rapidly diffuse between sensitizers via resonant energy migration, or be transferred less efficiently between energetically mismatched donor–acceptor pairs via phonon-assisted energy transfer.

The most common sensitizerion in lanthanide-based codoped UCNPs is Yb^{3+} as it has a comparatively large absorption cross section for NIR light for a Ln^{3+} ion. Moreover, its simple energy scheme consists of only a single emissive energy level, which reduces possible undesired nonradiative relaxation pathways of the excited state. The most frequently used activator ions are Er^{3+}, Tm^{3+}, and Ho^{3+}, with their manifold of energy levels that are responsible for the multiple emission bands observed in UCNPs [19]. Figure 1 shows exemplarily the NIR-to-UV/visible UC mechanism of β-$NaYF_4$:Yb^{3+},Er^{3+}, one of the most efficient UC materials known to date [21, 22].

The 4*f* orbitals of Ln^{3+} ions are shielded by the completely filled $5s^2$ and $5p^6$ subshells, rendering the spectral position of the line-like sharp emission bands of UCNPs insensitive to the Ln^{3+} microenvironment. The intensity ratios of the different emission bands can, however, be affected by the Ln^{3+} microenvironment as well as by other parameters such as temperature, dopant concentration, and P as detailed in the following sections. Moreover, the parity-forbidden 4*f*–4*f* transitions of Ln^{3+} ions account for the small absorption cross sections and low emission rates. The low brightness of UCNPs is principally disadvantageous, yet is counterbalanced for many (bio)analytical applications by the typically low background noise due to NIR excitation, minimizing background or

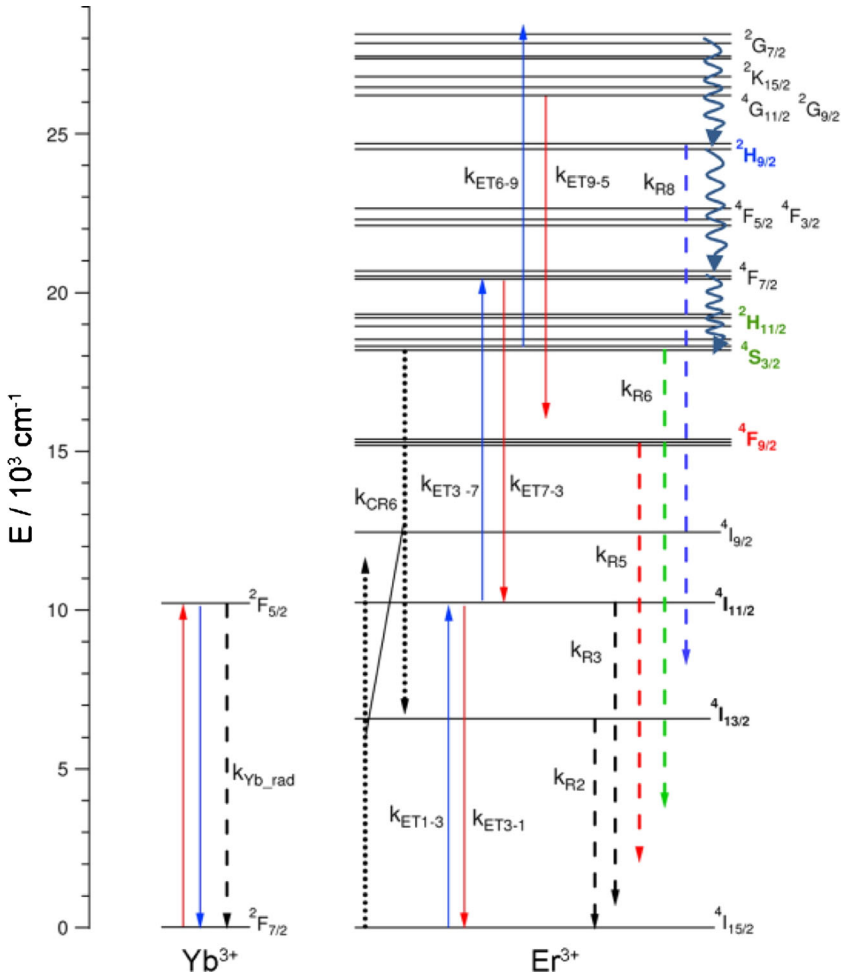

Fig. 1 Energy level diagram of the energy transfer upconversion mechanism in β-$NaYF_4$:Yb^{3+},Er^{3+}. Absorption of 980-nm light raises the sensitizer ion Yb^{3+} from its ground state $^2F_{7/2}$ to the excited level $^2F_{5/2}$. This transition is reversible, and Yb^{3+} can emit near-infrared (NIR) light (*dashed black arrow*) with a (slow) rate constant k_{Yb_rad}. The absorbed energy can be reversibly transferred from Yb^{3+} to the activator Er^{3+} (*blue arrow* and *red arrow*) by dipole–dipole energy transfer. Once an Er^{3+} is in its excited state, it can be pumped into higher-energy states by additional dipole–dipole energy transfer processes from excited Yb^{3+} at neighboring lattice sites. Each energy transfer process depicted in this scheme is characterized by a distinct rate constant k_{ETx-y}. Radiative relaxation of Er^{3+} leads to the emission of green, red, and—to a lesser extent—blue light, indicated by d*ashed lines in the respective colors* with rate constants k_{Rx}. k_{CR} is the rate constant for Er^{3+}–Er^{3+} cross relaxation, a luminescence quenching processes requiring the proximity of two Er^{3+} ions. The *curvy arrows* indicate multiphonon relaxation from the different excited energy levels. (Adapted with permission from [21])

autofluorescence (e.g., in complex matrices containing other shorter-wavelength-absorbing fluorophores). Hence, depending on the respective application, either the absolute signal size determined by reporter brightness, or the signal-to-noise ratio is more relevant for analyte detection or discrimination. The parity (Laporte)-forbidden 4*f*–4*f* transitions of Ln^{3+} ions, which are commonly also spin multiplicity (spin multiplicity rule) forbidden, are also responsible for the long excited-state lifetimes (Table 1), which are the prerequisite for the sequential absorption of low-energy photons, which is, for example, 11 orders of magnitude more efficient than second harmonic generation [18]. Although the long excited-state lifetimes of Ln^{3+} ions are usually presented as an advantage for optical studies, this implies automatically a reduced number of emitted photons per time interval (slow photocycle) compared with fluorophores with luminescence lifetimes in the nanosecond range, and hence longer measurement times [23]. This afterglow can also affect measurements with a conventional scanning microscope (possible cross talk between pixels).

The unique photophysics of UCNPs and their advantages in various analytical and imaging applications have been covered by many review articles [4, 24–29]. They are also subject to the second part of this review series [insert citation of part II] focusing on applications in assays and sensors, yet UCNPs have also been shown to be very useful for photodynamic therapy [30–33], optical trapping [34, 35], and solar cells, which convert almost the full solar spectrum into a photocurrent [9, 36–38], and anticounterfeiting [39]. Here, we discuss possible solutions to the shortcomings of UCNPs such as their low brightness, the strong absorption of 980-nm light by water, and the challenging characterization of their application-relevant optical properties.

Rational design of monodisperse and bright UCNPs

At the very heart of UC nanotechnology are synthetic protocols that yield UCNPs with a homogeneous and narrow size distribution and a pure crystal phase with minimal lattice defects with a high batch-to-batch reproducibility because these features are fundamental for the brightness (*B*; see "UCL enhancement and color tuning") of UCNPs. This should ideally be available for a wide range of sizes. These features are affected by different synthesis parameters such as temperature, ligand-to-solvent ratio, and doping ions (lanthanide ions including Gd^{3+}, alkaline earth metal ions). UCNPs are typically synthesized by thermal decomposition, hydrothermal synthesis, coprecipitation, and ionic-ligand-based, microwave-assisted, and emulsion-based methods [40], and it is well known that the type and dopant concentration in the host matrix can influence nanocrystal shape, crystal phase, and crystal size [41]. Many different synthetic procedures have been reported that can be more or less easily upscaled [3, 29, 42, 43]. The synthetic methods used for UCNP production often differ, however, from publication to publication and from research group to research group; this, together with general difficulties to characterize the optical properties of UCNPs, summarized in the following section, are partly responsible for results that vary between research groups for each method.

Gainer and Romanowski [42] recently published a comprehensive guide to the synthesis of UCNPs, which includes the thermal decomposition of Ln^{3+} oleate and trifluoroacetate precursors and coprecipitation. These methods yield fewer toxic by-products and require less extreme temperatures, yet also lead to a lower quality of UNCPs and often require additional annealing steps to achieve good luminescence properties [42]. In addition, a protocol for the preparation of core–shell $NaGdF_4$ nanoparticles that incorporate Ln^{3+} ions into different layers for efficiently converting a single-wavelength, NIR excitation into a tunable visible emission that yields core–shell UCNPs within 1 day was reported by Wang et al. [44]. This protocol details the synthesis of core–shell $NaGdF_4$ nanoparticles grown through coprecipitation in a binary solvent mixture of oleic acid and 1-octadecene with the doping with lanthanides of controlled compositions and concentrations realized during particle growth. The Ln^{3+}-doped $NaGdF_4$ nanoparticles then serve as seed crystals for subsequent epitaxial growth of shell layers comprising different Ln^{3+} dopants. Other well-established and upscalable procedures have been reported, for example, by Haase and Schäfer [19] in 2011 and by Wilhelm et al. [45] in 2015. Moreover, the Haase group only recently developed an upscalable synthesis for the preparation of 10-nm β-$NaYF_4$:Yb,Er/$NaYF_4$ core–shell UCNPs with 5-nm particle cores that efficiently suppresses undesired nucleation of β-$NaYF_4$ particles during shell growth by using α-phase particles with a low ratio of sodium to Ln^{3+} ions [46].

Relatively new trends in the synthesis of UCNPs, which are closely related to concepts to boost UCNP brightness detailed in the next section [47], involve the development of synthetic procedures that reduce the mixing of core and shell material [48], and particularly the epitaxial growth of core–shell structures and engineering of homogeneous doping based on a successive layer-by-layer method with monolayer precision [49, 50]. This is expected to provide control of the local doping concentration and distribution of dopant ions in UCNPs, thereby minimizing deleterious CR and concentration quenching between dopants caused by too high local dopant concentrations and preventing local energy transfer barriers between sensitizer and activator ions, which can arise from low local dopant concentrations. The potential of this concept is highlighted in Fig. 2 for $NaGdF_4$:Yb^{3+},Er^{3+}/$NaYF_4$ UCNPs. This figure compares the luminescence properties of UCNPs obtained by a conventional synthetic approach yielding heterogeneous doping (referred to here as heterogeneous doping core UCNPs) and a homogeneous doping strategy (fabricating so-called

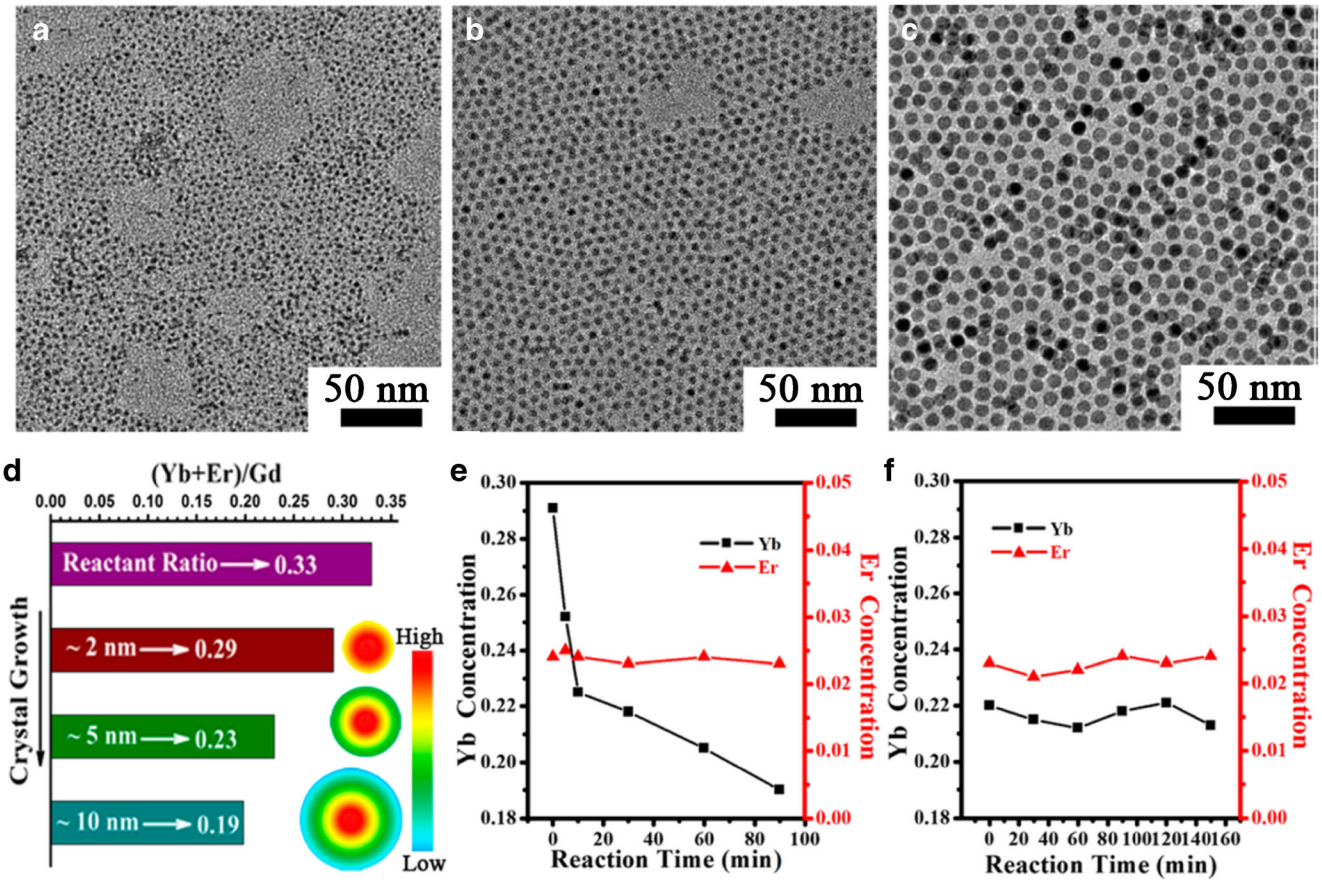

Fig. 2 Transmission electron microcopy images of $NaGdF_4$:Yb,Er photon-upconversion nanoparticles (UCNPs) obtained by the most commonly used one-pot heating-up method (heterogeneous doping core UCNPs) during particle spontaneous growth at different reaction times: **a** 5 min, **b** 30 min, and **c** 100 min. **d** Total doping concentration of Yb^{3+} and Er^{3+} determined by energy-dispersive X-ray spectroscopy at different growth stages of the spontaneous growth process. Evolutions of Yb^{3+} and Er^{3+} doping concentrations during spontaneous growth (**e**) and the successive layer-by-layer doping process (**f**) obtained by inductively coupled plasma atomic emission spectroscopy. The doping concentrations are evaluated with molar concentration. (Adapted with permission from [50])

homogeneous doping core UCNPs) using the one-pot successive layer-by-layer method [50] as demonstrated by the analytical characterization of these UCNPs and single-particle spectroscopy. Figure 2e reveals that in the case of the former synthetic method, the Yb^{3+} concentration gradually decreases from about 29% to 19% from inside to outside. Control of these approaches requires, however, also analytical methods to map and discern the homogeneity or heterogeneity of the respective core–shell structures on a single-particle level [47]. This presents a considerable challenge. Moreover, this underlines that the UCNP doping concentration cannot be reliably deduced from the macroscopic reactant feed ratio used for particle preparation.

UCL enhancement and color tuning

The brightness (B) of UCNPs is the product of the material's molar absorption coefficient [$\varepsilon(\lambda)$, or absorption cross section, $\sigma_{abs}(\lambda)$] at the excitation wavelength (λ_{ex}) [51], which is a measure of the absorption strength in the case of nanoparticles, and the photoluminescence quantum yield (Φ_f), a measure of the luminescence efficiency. The definition and determination of the UC fluorescence quantum yield of UCNPs (Φ_{UC}) are addressed in a separate section [52]. Hence, for high signals and low detection limits, generally all factors that yield high $\sigma_{abs}(\lambda)$ and/or Φ_{UC} or increase the values of both parameters are beneficial. Depending on the respective application, the signal-to-noise or background ratio can also provide an important measure here, thereby at least partly counterbalancing the low brightness of NIR-excited UCNPs.

The brightness of UCNPs is mainly governed by (1) the host matrix—that is, its crystal phase (and hence also phase purity) and crystal structure that determine the local symmetry and crystal field sensed by the absorbing and emitting Ln^{3+} ions—as well as its phonon energy and (2) the choice of optimum (co)-dopant ion concentrations and the spatial arrangement of different Ln^{3+} ions in core-only and increasingly sophisticated core–shell architectures [47], thereby optimizing absorption cross sections and energy transfer processes and

preventing CR, a possible luminescence quenching pathway, as well as size-dependent surface quenching. Factors contributing to size-dependent surface quenching include surface defects (e.g., crystal defects or impurities) and ligands and/or solvents/matrices with high-energy vibrational modes [e.g., O–H vibrations at 3300–3700 cm^{-1} and $(CH)_n$ stretching vibrational modes at 2800–2950 cm^{-1}], which match with energy gaps between the manifold of energy levels of the Ln^{3+} dopant ions [53–56]. This originates from the relatively higher number of crystal defects found for smaller particles, which dissipate the excitation energy of the dopant ions, and the relatively larger number of surface Ln^{3+} ions. In addition to the chemical nature of the dopant ions, these nonradiative deactivation channels can also affect UCNP emission color.

Although UCNPs with core–shell architectures can be prepared with a very narrow particle size distribution, well-defined crystal morphology [57], control of dopant ion concentration [55], and surface chemistries providing water dispersibility [8, 58, 59], it is not completely clear yet why smaller UCNPs are produced at the expense of much weaker UCL. Typically, the UC efficiency even of UCNPs with optimized core–shell structures [60–62] is still about one order of magnitude lower than that of UC bulk materials, particularly for UCNPs dispersed in water [53–56]. This, together with the relevance of aqueous environments for all life science applications, has initiated a threefold response:

1. An increasing number of quantitative studies on the quenching of the UCL using steady-state and time-resolved fluorescence spectroscopy have been performed [53, 58, 63–65]. Material parameters assessed included the influence of the crystal phase and shell tightness as well as phonon coupling between the host lattice and the sensitizer (Yb^{3+}) as well as the activator (Er^{3+}), here with UCL measurements at ultralow temperatures [10, 66].
2. The design of an ever-increasing number of sophisticated core–shell particle architectures that utilize passive (i.e., protective-only) shells made from materials with identical or closely matching lattice constants as the core host and active shells comprising these materials containing different Ln^{3+} dopants, precisely arranged around the Ln^{3+}-doped core [53, 56], was triggered. These architectures passivate lattice defects at the core surface and protect excited sensitizer and activator ions from quenching by surface defects and high-energy vibrational modes outside the particle [57]. Active shells provide nanoscopic control of ion–ion interactions through spatial confinement of different types of Ln^{3+} ions in separate shell layers [47]. The design and preparation of these different types of hierarchical core–shell UCNPs was recently reviewed by Chen et al. [47].
3. Different strategies to enhance the absorption and/or luminescence efficiency have been assessed, such as sensitization with different inorganic and organic absorbers and plasmonic interactions.

An overview of concepts to improve UCNP brightness is highlighted in Fig. 3 [62]. These different strategies and underlying concepts are detailed in the following sections, except for photonic crystal engineering. Moreover, the potential of high *P* excitation (saturation excitation) to counterbalance UCL quenching is highlighted.

Surface passivation: UCNPs with passive and active shells

Minimization of surface quenching [67] can be realized with the aid of an inactive protective shell. As systematically studied, for example, by Wang et al. [55] in 2010 and Zhang et al. [68] in 2012, this requires sufficiently thick and closed shells [69, 70], passivating surface defects and shielding Ln^{3+} ions at the particle surface. Here, anisotropic shell growth [70], intermixing of core and shell material [48], and nucleation of particles from shell material [46] should be ideally prevented. Moreover, for optimum performance of core–shell architectures, compressive lattice strain should be minimized as this can also affect UC performance [71]. In the case of Förster resonance energy transfer (FRET) applications, shell thickness has to be compromised between high FRET efficiency and low surface quenching—that is, optimum UC efficiency (and optimum donor quantum yield, here Φ_{UC} of the UCNPs)—as demonstrated by Wang et al. [57].

Undoped shells have been made from silica, here also to facilitate subsequent surface functionalization and bioconjugation, and increasingly from common host materials such as $NaYF_4$ as well as from CaF_2 or SrF_2 [47]. In any case, questions arise here regarding shell tightness. For example, Chen et al. [70] demonstrated recently the strong influence of the size of the hexagonal Yb^{3+}/Er^{3+}:$NaGdF_4$ core on the morphology and growth of a complete (i.e., close) surface-passivating shell on the UCNP core for core sizes of 9.5, 16.2, 20.4, and 31.5 nm. As the shell growth mechanism, Chan et al. used separate nucleation of the shell precursors followed by ripening-mediated deposition on UCNP cores. The choice of appropriate core sizes for optimum shell growth can lead to a very strong increase in UCL intensity, with factors of up to 10^4 compared with the core without a shell having been reported [70]. These high enhancement factors were determined by comparison of the UCL intensity with the directly (at 490 nm) excited intensity of the (DC) with a spectrofluorometer equipped with an integrating sphere for low *P* of about 1.5 W cm^{-2} (at 980 nm) [69]. Also Qiu et al. [69] claimed a strong UCL amplification for Yb^{3+}/Er^{3+}:$NaGdF_4$@$NaYF_4$ core–shell UCNPs with a completely closed shell. Fischer et al. [58] recently reported precise engineering of core–shell UCNPs, and derived a correlation between luminescence efficiency and shell thickness. This is

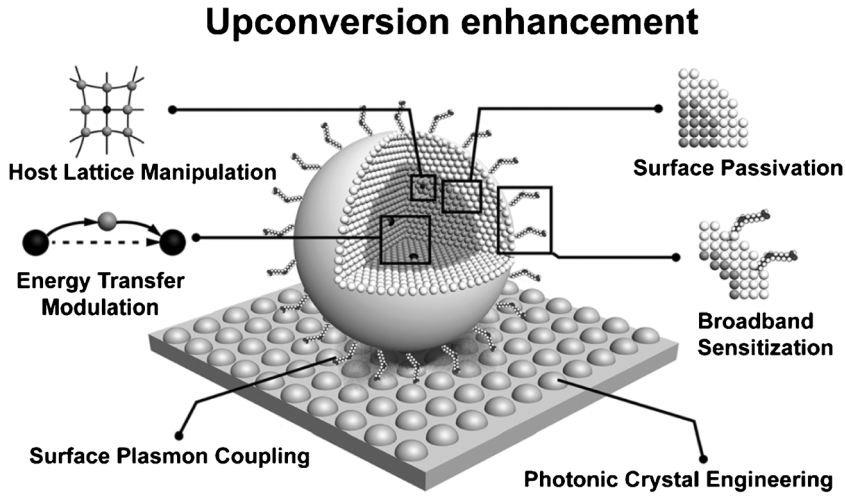

Fig. 3 Overview of the main strategies for enhancing luminescence in Ln^{3+}-doped UCNPs. Often, upconversion luminescence enhancement is realized synergistically by a combination of different concepts. (Adapted with permission from [62])

highlighted in Fig. 4. Here, maximum UCL efficiency was obtained for an optimized shell thickness of about 4 nm with use of an integrating sphere setup for UCL measurements. These authors also determined surface quenching rates for the relevant Er^{3+} and Yb^{3+} energy levels and used this knowledge to prepare UCNPs showing surface-quenching-assisted efficient NIR to short-wavelength infrared (SWIR) downshifting (i.e., strong Er^{3+} emission at 1520 nm on excitation at 980 nm) [58].

An increasingly used concept for enhancing UCL is directed energy migration in sophisticated multishell structures (see also "Co-doping with Nd^{3+}" and "Broadband sensitization with organic dyes and energy transfer modulation"). This has been realized, for example, by Qiu et al. [69] for Yb^{3+}/Tm^{3+}-co-doped fluoride active core–active shell–inert shell nanoparticles. Wang et al. [72] showed for Gd^{3+}-based UCNPs of various composition how the rational design of a core–shell structure with a set of Ln^{3+} ions incorporated into separated layers at precisely defined concentrations can be used to fine-tune UCL and enhance UCL efficiency through trapping of the migrating energy by the activators and prevention of unfavorable CR. Other approaches to color tuning or color control exploit strain-induced modulation of the (de)population channels of excited energy levels of UCNPs or CR. For example, on the basis of the former, Ye et al. [53] converted the green, yellow, and blue luminescence of Yb^{3+}/Ho^{3+}-, Yb^{3+}/Er^{3+}-, and Yb^{3+}/Tm^{3+}-co-doped $NaYF_4$ into a quasi-white, green, and pink-blue emission in the respective sensitizer/activator-isolated $NaYF_4$ core–shell nanostructures: $NaYF_4$:Yb^{3+}@$NaYF_4$:Ho^{3+}, $NaYF_4$:Yb^{3+}@$NaYF_4$:Er^{3+}, and $NaYF_4$:Yb^{3+}@$NaYF_4$:Tm^{3+}. An elegant example of the use of Er^{3+}–Er^{3+} CR for color tuning in core–multishell structures was reported by Wei et al. [73] for the generation of pure red UCL in activator- and sensitizer-rich UCNPs.

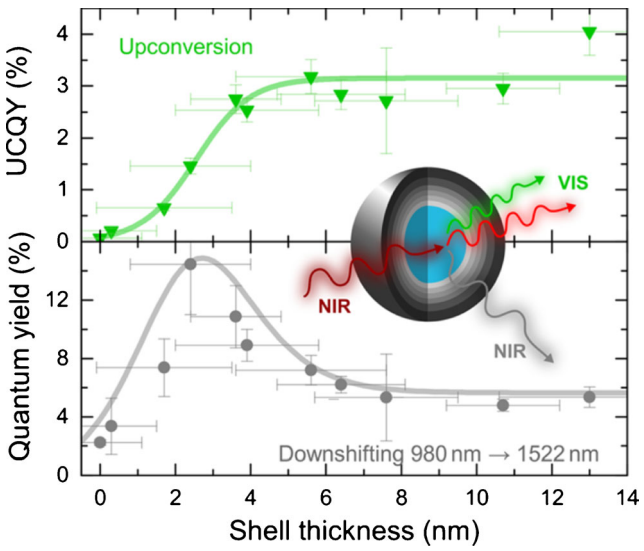

Fig. 4 Influence of shell thickness on the quantum yield of upconversion luminescence (*UCQY*; *top*) and the quantum yield of the Er^{3+} emission at 1520 nm (downconverted emission; *bottom*). (Reprinted with permission from [58])

Host lattice manipulation and co-doping with transition metal ions

As UCL depends strongly on the crystal phase of the host matrix [45], the local crystal field faced by the Ln^{3+} ions in the host matrix [74], and Ln^{3+}-Ln^{3+} distances determined by the host lattice and doping ion concentration (see also "Improving the excitation efficiency of UCNPs") [41], tailoring of these parameters can present effective ways to increase UCL by factors of several ten. It can be also used for UCL color tuning. The most commonly used strategy for altering crystal field symmetry involves co-doping with the very small alkali metal ion Li^+, which is built into the host lattice substitutionally or interstitially [75–77]. Co-doping has been also done with other transition metal ions such as Sc^{3+}, which has a

slightly smaller ionic radius than Y^{3+}, and recently also with, for example, Mn^{2+} and Fe^{3+} [24, 78–80]. Moreover, emission colors can be selectively enhanced by co-doping and tuning of the population of certain emissive energy levels as demonstrated, for example, by Fe^{3+} co-doping of $NaYF_4$:Yb^{3+},Er^{3+} nanocrystals [78]. This led to amplification of red UCL.

To interpret these literature data, it has to be kept in mind that for some systems showing (co)-doping-induced intensity boosting and/or color tuning, UCNP doping concentration is obtained solely from the reactant feed ratio used for nanocrystal synthesis, which must not match with the actual dopant ion concentration built into the host lattice. The type of doping ions can also significantly affect the crystal phase (see also "Rational design of monodisperse and bright UCNPs"), and hence via this parameter also UCL, in addition to, for example, ion–ion interactions. Moreover, often little attention is paid to dopant ion distribution on the single-particle level [50]. Generally, a homogeneous distribution of dopants is expected to minimize concentration quenching and thus improve the optical properties and overall quality of UCNPs. The question of whether the doping Ln^{3+} ions are statistically distributed in a single nanoparticle and how much individual UCNPs in an ensemble of particles differ can be addressed with the aid of advanced imaging techniques such as scanning transmission electron microscopy operated in high-angle annular dark-field imaging mode, which is sensitive to the atomic number (Z) of the sample (scaling proportionally to Z^2), combined with electron energy loss spectroscopy and energy-dispersive X-ray spectroscopy [47, 69]. This makes possible spatially resolved characterization of core–shell structures (relevant for assessing shell closeness) and dopant ions on the single-particle level. This underlines the importance of synthetic strategies that provide homogeneous doping in core and core–shell structures in conjunction with the need to better control shell growth. Interesting approaches to this problem could be the method recently reported by the Haase group [46] for preparing gram amounts of very small $NaYF_4$:Yb^{3+},Er^{3+}@$NaYF_4$ UCNPs with suppression of undesired nucleation of β-$NaYF_4$, and the use of a layer-by-layer deposition method as recently reported by Li et al. [50] for the synthesis of $NaGdF_4$:Yb^{3+},Er^{3+} UCNPs. These authors also studied the influence of spatial distributions and relative concentrations of the dopants on the optical properties of UCNPs for the first time at the single-nanoparticle level. In addition to these pitfalls arising from UCNP synthesis, for many of the reported UCL amplification factors, the reliability of the underlying UCL measurements needs to be carefully estimated, thereby considering criteria detailed in "Quantitative spectroscopic studies of UCL and Φ_{UC} and challenges." Particularly, relative fluorescence measurements can be error-prone and are, for example, strongly affected by differences in scattering properties and P. Generally, only nonaggregated systems of closely matching size are to be compared.

Improving the excitation efficiency of UCNPs

Another factor responsible for the low brightness of UCNPs is the very small absorption cross sections of Ln^{3+} ions due to the parity-forbidden and in most cases also spin-multiplicity-forbidden *f–f* transitions in conjunction with the very narrow absorption bands. For example, the commonly used Ln^{3+} sensitizer ion Yb^{3+} absorbs light with a critically small absorption cross section of approximately 10^{-20} cm^2, which is about 1000−10,000 times less than that of a dye molecule, revealing typically an absorption cross section of about 10^{-17}–10^{-16} cm^2, in a narrow spectral window of approximately 10,260 −10,660 cm^{-1} (approximately ten times narrower than that of an organic dye) [81]. To improve the excitation efficiency of UCNPs, different strategies have been pursued, such as the modulation of the Ln^{3+} activator concentration, co-doping with Nd^{3+}, and dye sensitization, which are discussed in this section. The latter two concepts also shift the excitation wavelength from 980 nm to 808 nm or allow increased flexibility in the excitation wavelength, thereby minimizing water absorption at the excitation wavelength.

Modulating the Yb^{3+} sensitizer concentration

To boost UCNP brightness, the Yb^{3+} concentration can be increased, particularly because Yb^{3+} ions have a lesser tendency for concentration-dependent quenching compared with other Ln^{3+} ions because of their simple energy level scheme (see Fig. 1). This enhances not only the absorption cross section of the UCNPs, but also affects all distance-dependent energy transfer processes involved in the generation of UCL (see Fig. 1), such as Yb^{3+}–Yb^{3+} interaction-related energy migration and the probability of the energy transfer from Yb^{3+} to the activator ions. This, in conjunction with the interest in color tuning, triggered several studies on the influence of Yb^{3+} concentration and Yb^{3+}/Er^{3+} or Yb^{3+}/Tm^{3+} doping ratios for differently sized $NaYF_4$, $NaGdF_4$, and GdF_3 UCNPs [41, 82–84].

For example, Chen et al. [82] increased the concentration of the sensitizer Yb^{3+} from the typically used 18% or 20% up to 100% in a series of ultrasmall $NaYF_4$:Yb^{3+}/Tm^{3+} nanocrystals with sizes of 7–10 nm. Along with an increase in the relative content of Yb^{3+} ions from 20% to 100%, with a corresponding decrease in Y^{3+} content from 80% to 0%, this resulted in an increase of NIR UCL by a factor of 43. These ultrasmall $NaYbF_4$:2% Tm^{3+} nanocrystals had a 3.6 times more intense NIR emission than 25–30-nm $NaYF_4$:20% Yb^{3+}/2% Tm^{3+} UCNPs previously synthesized by this group. Although this enhancement does not solely arise from the increase in absorption cross section, this factor is expected to considerably contribute to this effect. Structural and photoluminescence studies of a series of 20-nm to about 100-nm β-$NaGdF_4$ nanocrystals revealed an influence of

relative Yb^{3+}/Tm^{3+} [83] and Yb^{3+}/Er^{3+} [41] concentration on size, size distribution, and morphology and as to be expected on the contribution of the different emission bands to overall UCL, reflecting ion–ion interactions, including CR. These concentration dependences and the size-dependent and dopant-concentration-dependent probability for cluster formation (e.g., Yb^{3+}–Er^{3+}–Yb^{3+} as well as Yb^{3+} and Er^{3+} cluster formation) were also modeled and correlated with experimentally observed green-to-red intensity ratios [41]. These results revealed that for UCNPs with sizes exceeding 20 nm, ion–ion interactions and not particle size are the main factors governing their optical properties.

Yb^{3+} is commonly excited at 980 nm, where the absorption of water and other tissue components is not negligible. This can result in laser-induced local overheating effects in cell, tissue, and live animal studies. Hence, particularly for all in vitro and deeper in vivo bioimaging applications of UCNPs, shifting of the excitation wavelength from 980 nm to shorter wavelengths such as 915 nm or 808 nm, where absorption of water and tissue components is lower, can be attractive. For example, pioneering work on excitation-wavelength-dependent overheating effects was done by the group of Anderson-Engels [85]. By measuring the thermalgraphic maps of a mouse in response to laser excitation at 980 nm and 915 nm using $Tm^{3+}/Er^{3+}/Ho^{3+}$-doped $NaYbF_4$ UCNPs, they demonstrated the superiority of 915-nm excitation for bioimaging applications, with less heating of the biological specimen and larger imaging depth in animals or tissues. This triggered the search for design strategies providing bright UCNPs excitable at wavelengths different from 980 nm.

Co-doping with Nd^{3+}

Nd^{3+}, which has a relatively high absorption coefficient compared with most other Ln^{3+} ions, has been used as a substitute for Yb^{3+} to shift the excitation wavelength from 980 nm to 808 nm as well as in combination with Yb^{3+}. An increasing number of Nd^{3+}-based UCNPs differing in core and shell design and host matrix have emerged [61, 77, 86–91]. An example of introducing Nd^{3+} as a sensitizer and building a core–shell structure to ensure successive Nd^{3+}-> Yb^{3+}-> activator energy transfer was reported by Wang et al. [86], who demonstrated the potential of these Nd^{3+}-doped UCNPs in in vivo imaging experiments together with a strongly reduced laser-induced local overheating effect. Also $Nd^{3+}/Yb^{3+}/Ln^{3+}$-tridoped UCNPs have been reported, where the Nd^{3+} ions act as primary sensitizers and 800-nm absorbers, and the Yb^{3+} dopants serve as bridging sensitizers to facilitate energy transfer from Nd^{3+} to the activator ions (Nd^{3+}–Yb^{3+}–Ln^{3+} energy transfer cascade).

The luminescence of simple Nd^{3+}/Yb^{3+}-based UCNPs on 808-nm excitation is nevertheless often less efficient than that of their Yb^{3+}-based counterparts excited at 980 nm, particularly in simple Nd^{3+}-based systems, as the Nd^{3+} ion has a much more complicated energy level diagram compared with the Yb^{3+} ion [91], with its favorably simple energy level diagram shown in Fig. 1. Consequently, the Nd^{3+} doping concentration must be kept very low (up to 1 mol%) in $Nd^{3+}/Yb^{3+}/Ln^{3+}$ tridoped UCNPs, rendering the absorption of these UCNPs at 808 nm only weak. Higher doping concentrations of Nd^{3+} can induce deleterious CR energy transfer between Ln^{3+} activators and Nd^{3+} ions, leading to a reduction in UCL efficiency. An effective design concept to enhance UCL of Nd^{3+}/Yb^{3+}-based UCNPs, sensitized by cascade energy transfer, was developed by Huang and Lin [91], who designed active-core–active-shell nanomaterials by refining the concept of Xie et al. [87]. They grew an active Nd^{3+}-doped shell (doping concentration of 20 mol% for effective light harvesting) made from a material with similar lattice constants as the core, around the $NaYF_4$:$Nd^{3+}/Yb^{3+}/Er^{3+}$ (1/19/0.5; 1 mol% Nd^{3+}) core, which protects the luminescent core from surface quenching and efficiently absorbs NIR light as shown in Fig. 5. To enhance energy transfer from Nd^{3+} to bridging Yb^{3+}, the shell was co-doped with Yb^{3+}. This design concept led to $NaYF_4$:$Nd^{3+}/Yb^{3+}/Er^{3+}$@$NaYF_4$:Nd^{3+}/Yb^{3+} active-core–active-shell UCNPs with (claimed) luminescence enhanced by factors of 522 and 2.6 compared with $NaYF_4$:$Nd^{3+}/Yb^{3+}/Er^{3+}$ core-only and $NaYF_4$:$Nd^{3+}/Yb^{3+}/Er^{3+}$@$NaYF_4$:Nd^{3+} active-core–active-shell UCNPs respectively. This design strategy works also for the Tm^{3+} activator [91]. Nevertheless, up to now, the overall success of this design concept has not been too impressive.

Broadband sensitization with organic dyes and energy transfer modulation

An increasingly used concept to boost the molar absorption cross section is sensitization with NIR organic dyes, which allow also tuning of the excitation wavelength. This provides more flexibility with respect to the choice of excitation light sources and allows the minimization of heating effects in bioimaging studies due to tissue absorption. Broadband dye-sensitized UCL was first shown by Zou et al. [91] by adding a carboxylic acid derivative of the dye IR-806 to a solution of oleylamine-coated β-$NaYF_4$:Yb^{3+},Er^{3+} UCNPs in chloroform. The observed strongly amplified UCL was attributed to FRET from excited IR-806 to the Yb^{3+} and Er^{3+} energy-accepting ions in the β-$NaYF_4$:Yb^{3+},Er^{3+} nanoparticle core. As revealed by control experiments with a dye lacking a carboxylic acid group, dye sensitization clearly required binding of the NIR dye to the particle surface. This concept of antenna dyes has been further refined since then. Recent examples from the Chen and Prasad group [78, 92] include hybrid inorganic−organic systems consisting of epitaxial core–shell UCNPs and NIR dyes anchored on the core–

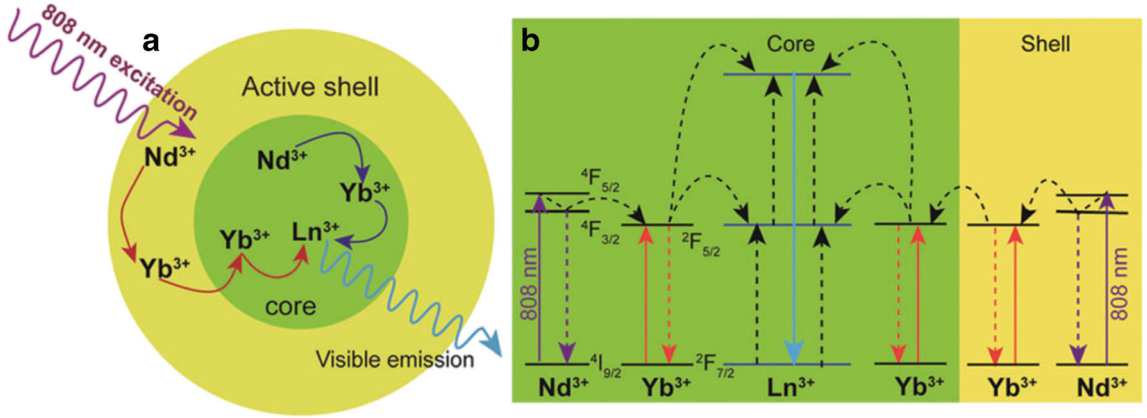

Fig. 5 **a** The active-core–active-shell nanoparticle architecture for photon upconversion on 808-nm laser excitation. Nd^{3+} and Yb^{3+} ions are simultaneously co-doped in both the core and the shell, and act as co-sensitizers to absorb the excitation energy and subsequently transfer it to the Ln^{3+} activator ions (e.g., Er^{3+} or Tm^{3+}). **b** The energy transfer mechanism in these active-core–active-shell UCNPs. (Reprinted with permission from [91])

shell nanocrystal surface. These nanostructures exhibit multi-step cascade energy transfer from the broadly absorbing NIR organic dyes to the sensitizer ions in the epitaxially grown shell, followed by sequential nonradiative energy transfer to upconverting ion pairs in the core as highlighted in Fig. 6 [92].

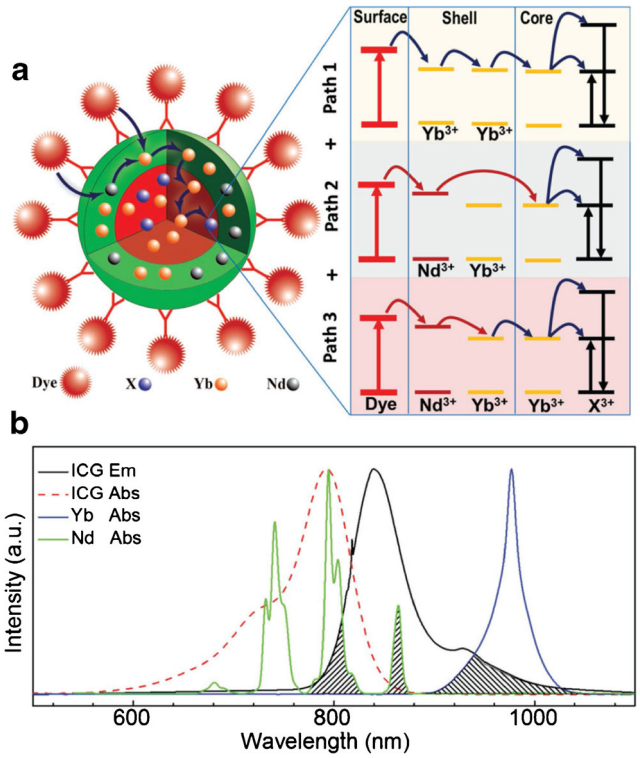

Fig. 6 Multidimensional energy cascaded upconversion in dye-sensitized core–active-shell $NaYF_4:Yb^{3+}/X^{3+})@NaYF_4:Nd^{3+}/Yb^{3+}$nanocrystals. **a** Multidimensional energy transfer pathways from the NIR dye molecules on the particle surface to the Ln^{3+} ions in the core. **b** Absorption (*dashed red line*) and emission (*solid black line*) spectra of the NIR dye indocyanine green (*ICG*) and absorption spectra of Nd^{3+} (*solid green line*) ions and Yb^{3+} (*solid blue line*) ions. (Adapted with permission from [93])

In these core−shell architectures, surface-related UCL quenching is suppressed, yielding a high Φ_{UC} of 4.8%. This exceeds typically reported UCNP efficiencies at 800 nm by a factor of about 100. Such UCNPs can be excited in a broad NIR wavelength region (more than 150 nm) with a large $\sigma_{abs}(\lambda)$ of 1.47×10^{-14} cm^2 per single nanoparticle [78].

Dye sensitization was also used for the tailoring of the excitation bands of dye-sensitized UCNPs to realize excitation-wavelength-selective imaging [94]. For example, 20-nm β-$NaYF_4$:20% Yb^{3+},2% Er^{3+} nanoparticles were treated with nitrosonium tetrafluoroborate to remove hydrophobic organic ligands remaining from the synthesis and were subsequently coated with different concentrations of a series of NIR dyes (IR-783, IR-808, IR-820, and IR-845), with systematically increasing absorption wavelengths. Significantly enhanced UCL was also achieved by Wu et al. [95] by their combining dye sensitization with protective shells in dye-sensitized core–active-shell UCNPs. Here, the UCNP shell was doped with Yb^{3+} ions to bridge energy transfer from the NIR dye to the UCNP core. Such materials are of interest for imaging as well as security applications [96].

For all concepts and applications involving FRET with UCNPs, it must be kept in mind that each UCNP consists of a large number of individual emissive lanthanide ions with multiple transition dipole moments [97]. Hence, UCNP FRET is substantially different from FRET between two organic dyes (ideally present in a 1:1 stoichiometry) or between semiconductor quantum dots and dyes [98] as photon UC involves energy transfer cascades between several Ln^{3+} ions and competition with nonradiative deactivation pathways.

Multicolor and high-energy excitation

UCNPs are used under quite different excitation conditions. For example, particularly in vivo studies are commonly performed at relatively low P ($P < 1$ W cm^{-2}) [99] and assays with

$P < 100$ W cm^{-2} [100, 101], with UCL being far from saturation. Mechanistic ensemble studies are increasingly done as a function of P (i.e., at P ranging from approximately 1 W cm^{-2} to approximately 5000 Wcm^{-2}) [102, 103]. Single-particle measurements with microscopic setups and focused lasers are performed at very high P ($P > 10^5$ W cm^{-2} up to about 5×10^6 Wc m^{-2}; saturation excitation) [104, 105]. Several research groups have recently demonstrated that UCL quenching can be partly overcome by higher P [102, 105]. For example, recent studies by Zhao et al. [103] revealed that high P can alleviate concentration quenching for higher activator concentrations, resulting in enhanced UCL. The resulting UCNPs were bright enough to allow remote tracking of very small single particles [103]. Studies by Gargas et al. [105] demonstrated that UCL quenching channels such as surface defects, which become critical at diameters below 20 nm, can be overcome by high P. This underlines that factors known to increase UCNP brightness in ensemble measurements lose relevance at the much higher P used for single-particle studies. High P is also amenable to color tuning, thereby exploiting the different photonic nature of the various emission bands and the manifold of population channels offered by the different energy levels of, particularly, the activator ions. Moreover, modulation of P by variation of the excitation repetition rate was used to control the green and red UCL in $NaYF_4$:Yb^{3+},Er^{3+} nanoparticles [106]. Saturation excitation was also used for the switching between two-photon and four-photon UC in Yb^{3+},Tm^{3+}-doped $NaYF_4$ nanoparticles on the single-particle level using very high P between 3.5×10^4 W cm^{-2} and to 1.1×10^7 W cm^{-2} [104]. Furthermore, recently, high P in conjunction with excitation at 980 nm and illumination at 808 nm has been even used for amplified stimulated emission in single Yb^{3+}/Tm^{3+}-co-doped $NaYF_4$ UCNPs with a dual-laser confocal microscope for super-resolution nanoscopy [107].

These phenomena could hardly be detected in ensemble measurements where the biphotonic $^3H_4$ level always dominates. Moreover, recently, Wang et al. [108] manipulated the spectral profile and lifetime of the Ln^{3+} emission in UCNPs by tailoring their nonlinear optical properties, using surface defect engineering and doping to enhance energy distributions and thereby the emitters' sensitivity to P. Another interesting approach to improve UCL efficiency is multiwavelength excitation. This was recently demonstrated for Er^{3+}-doped $NaYF_4$ nanoparticles [109]. Excitation of the green and red emission of these $NaYF_4$:1% Er^{3+} nanoparticles excited by two single wavelengths, 790 nm and 1520 nm, leads to emission enhancement by factors of 3.05 and 1.53 respectively, compared with the sum of the emission intensities resulting from two separate single-wavelength excitations. This observation was attributed to ground-state and excited-state absorption, and could suggest a solution for the efficient utilization of NIR light by solar cells.

Plasmonic enhancement

Plasmonic enhancement of UCL, or so-called plasmon-enhanced UC, aims at improving both absorption and emission processes in UC materials by tailoring the electric and magnetic fields at the position of the UC emitter with high-frequency electromagnetic resonances of electrons in conducting materials, commonly noble metal nanoparticles or shells [110, 111]. Typically, only electronic dipole transitions can be efficiently enhanced by plasmonic effects, whereas magnetic dipole transitions (most Ln^{3+} ions have mixed electronic and magnetic dipole transitions) are much less if at all affected.

Plasmonic effects exploit the fact that a plasmonic nanoantenna like a noble metal nanoparticle or a metal shell can influence a nearby emitter by (1) locally concentrating the incident field and enhancing absorption and (2) modifying the local density of energy levels, leading to faster radiative decay rates, thereby enhancing emission. Indicative of the latter are a concomitant shortening of the luminescence decay times and, in the case of UCNPs, also the rise times [112]. Moreover, plasmonic effects can quench the luminescence by increasing nonradiative decay rates. The interplay of these three processes depends on spectral overlap between the resonances and absorption/emission frequencies, field overlap, polarization, distances, antenna material, and pump power. Also, the intrinsic quantum yield of the emitter must be considered, with low quantum yields as found in Ln^{3+}-based UC emitters allowing greater enhancement. Compared with other materials, plasmonic effects in UC materials are further complicated by (1) the multistep nature of the UC processes involving long-lived intermediate states that each have competitive decay pathways, which can be all affected by plasmon resonances, (2) the interdependence of the populations of the excited states involved in UC, and (3) the P-dependence of the UC processes and the population and depopulation of the energy levels involved. Furthermore, the illumination of plasmonic structures can result in local heating effects that can also influence UCL.

Different UC–plasmonic nanostructures have meanwhile been realized with plasmon resonances matched to absorption (intensity enhancement in excitation) and to emission in different geometries [78, 113–117]. For (bio)analytical applications, typically core–shell architectures consisting of a UC core coated with a dielectric spacer layer consisting of, for example, silica or layer-by-layer assembled polyelectrolyte multilayers of a few nanometers up to several tens of nanometers in thickness covered with gold or gold nanoparticles (GNPs; spherical particles or rods) or a closed metal shell should be attractive [118, 119]. A summary of enhancements factors for different materials and different geometries taken from [110] is shown in Fig. 7. A comparison of the different approaches reported so far is, however, almost impossible

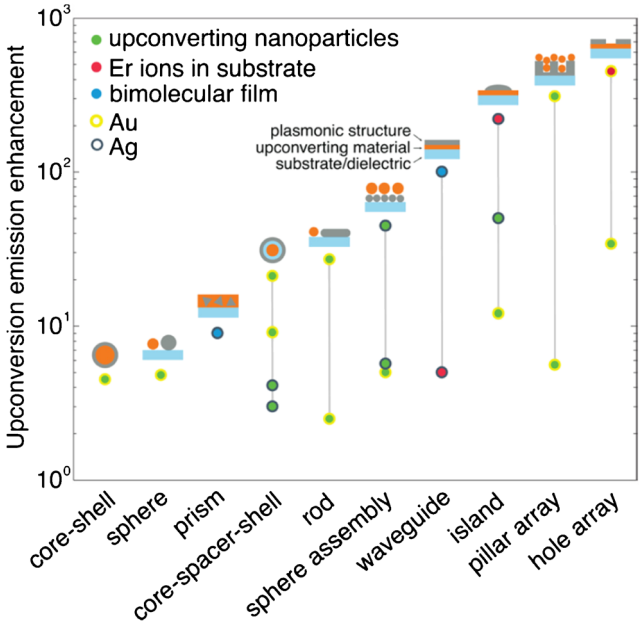

Fig. 7 Enhancement factors reported for two-photon upconversion from Ln^{3+}-doped UCNPs (*green dots*), Er^{3+}-doped substrates (*red dots*), and bimolecular films (*blue dots*) using a variety of plasmonic geometries. The plasmonic material is indicated with either a *yellow ring* (gold) or a *gray ring* (silver). Schematics of each geometry's cross section are included, with *gray* indicating a plasmonic material, *orange* indicating an upconversion material, and *blue* indicating a substrate or dielectric spacer. (Reprinted with permission from [110])

because of the variability in experimental parameters chosen and reported, particularly *P*, and the sometimes questionable characterization of the materials (see also "Quantitative spectroscopic studies of UCL and Φ_{UC} and challenges").

A very recent and interesting example of the simulation of the changes in the spontaneous emission of the UCL and the influence on the nonlinear UC processes is shown in Fig. 8, demonstrating the effect of 300-nm spherical GNPs (diameter of 300 nm) on the absorption, UCL, and Φ_{UC} of an upconverter in the vicinity of these GNPs, also considering different *P* [120]. This was realized with a comprehensive 3D computation-based approach using Mie and electrodynamic theory and a UC rate equation model. Regarding the still debated influence of plasmonic structures and local density of photon states on the rate of energy transfer UC, the most significant UC process for Ln^{3+}-doped UC materials, modified energy transfer rates caused by an altered decay rate of the donor or acceptor state were also considered. According to these simulations, the nonradiative losses are particularly strong at very short distances between the dipole emitter and the GNP, and reach 10% of the intrinsic spontaneous emission rate for distances larger than about 50 nm. UCL enhancement was optimum for a distance of about 35 nm to the GNP surface and UCL was strongly quenched for distances less than 40 nm. Maximum Φ_{UC} enhancement was determined to be 117% for the GNPs at a low incident *P* of 0.01 W cm^{-2} and decreased with increasing *P*. Moreover, Fischer et al. [120] clearly emphasized that depending on whether absorption, UCL, or Φ_{UC} is to be maximized, the UC material must be placed at positions different from the position of the plasmonic material.

Quantitative spectroscopic studies of UCL and Φ_{UC} and challenges

A major factor hampering the full exploitation of the application potential of UCNPs is the challenging characterization of their spectroscopic key features. The need to improve the optical properties of UCNPs, identify radiationless deactivation pathways, and develop optimum design strategies for brighter UCNPs is closely linked to quantitative studies of UCL and the availability of reliable UCL data and enhancement factors. This is particularly true for Φ_{UC} values, which provide a direct measure of the efficiency of the conversion of absorbed light into photoluminescence (UCL and DC luminescence with the latter being neglected). A definition of Φ_{UC} is given in Eq. 1:

$$\phi_{UC}(P) = \frac{N_{em}}{N_{abs}}, for \lambda_{em} < \lambda_{abs} \quad (1)$$

where N_{em} is the number of photons emitted with a wavelength $\lambda_{em} < \lambda_{abs}$, which is obtained from the integral emission intensities of all (spectrally corrected) UC emission bands (except for sensitizer luminescence), and N_{abs} is the number of photons absorbed [9, 52].

In contrast to linear emitters such as organic dyes or semiconductor quantum dots, which can come close to having Φ_f values of unity, it is evident from Eq. 1 that for a purely biphotonic process, Φ_{UC} can maximally converge to 0.5 in the case of saturation. Typically, Φ_{UC} is much smaller—on the order of about 10% for efficient bulk UC materials—and about a factor of 10 smaller for highly efficient UCNPs in a dispersion. This generally accepted measure of the luminescence efficiency of molecular and nanoscale emitters is particularly difficult to obtain for UC materials because of the multiphotonic nature of the excitation process, which introduces a dependence on *P* (see Eq. 1). Although the photoluminescence quantum yields of transparent solutions of conventional linear emitters such as organic dyes or semiconductor quantum dots can be principally measured relatively, by comparison of the absorption-weighted integral fluorescence intensities of a sample and a standard of known Φ_f using of a spectrofluorometer [121, 122], the *P*-dependence of Φ_{UC} makes absolute measurements with an integrating sphere mandatory [10, 123]. In this case, N_{em} is obtained from the integral emission intensities of all (spectrally corrected) UC emission bands (except for the sensitizer luminescence); N_{abs} results from the integrated difference of the spectrally

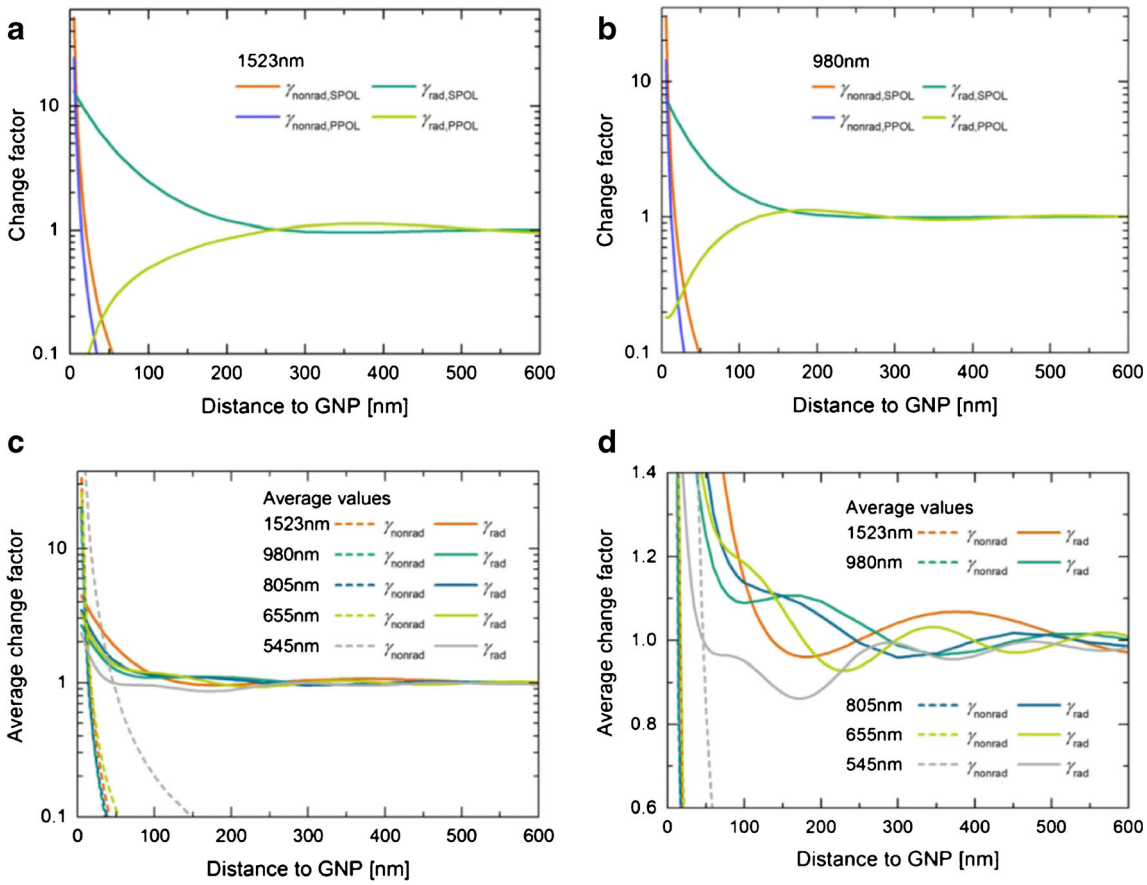

Fig. 8 Change factors of the spontaneous emission and additional nonradiative loss channels due to the presence of the spherical gold nanoparticles (*GNP*) for two different polarizations of the electric dipole emitter as a function of the distance to the GNP with a diameter of 300 nm for **a** 1523-nm and **b** 980-nm dipole emitters. **c** Radiative and nonradiative change factors averaged over the polarizations—that is, the orientation of the emitting dipole relative to the surface of the GNP, either parallel (*PPOL*) or perpendicular (*SPOL*)—and **d** an enlargement of the data from **c** to better visualize the values close to 1. The enhancement factors for the different nonradiative and radiative processes are represented by γ. (Adapted with permission from [120])

corrected measurement of the transmitted incident radiant powers of a blank (solvent or solvent and scatter) and the sample in the wavelength range of excitation [51, 52, 121, 122]. Moreover, P must also be precisely determined. The P-dependence of Φ_{UC} also imposes stringent requirements on the spatial homogeneity of the P distribution of the excitation beam profile used for Φ_{UC} measurements, which must be considered by an appropriate design of the measurement setup as only recently addressed in detail by Kaiser et al. for UCNPs dispersed in toluene [118]. Furthermore, a single Φ_{UC} value at a given P is not sufficient to characterize the performance of a UC material, for which knowledge of the P-dependence of Φ_{UC} and/or the saturated UCL quantum yield $\Phi_{UC,sat}$ is needed [7]. In addition to the challenging radiometric characterization of the integrating sphere, particularly the determination of the wavelength-dependent spectral responsivity, other pitfalls can arise from size- and wavelength-dependent scattering of the UCNPs [122], which can also affect the P distribution within the exited sample volume. Only such absolute or quantitative P-dependent measurements of UCL provide really accurate and comparable UCL spectra, intensity ratios (green-to-red intensity ratios), and photonic orders (equaling the so-called slope factor n, which gives the number of photons required for the population of an emissive energy level) of the respective UC emission bands for mechanistic insights into excited-state (de)population pathways of the different energy levels and assessment and improvement of material performance.

The complicated absolute measurement of UCL intensities and efficiencies together with the lack of commercial instrumentation such as a stand-alone integrating sphere setup for UCL affects the reliability of luminescence efficiencies, Φ_{UC} values, and/or luminescence enhancement factors reported in the literature. This makes a quantitative assessment and comparison of UCL enhancement strategies difficult. Presently, most Φ_{UC} values and enhancement factors are obtained from relative luminescence measurements with a spectrofluorometer or an integrating sphere [3, 124] with use of either an organic dye such as IR-26 [99] or another UC material [125] as the reference, although the suitability and limitations of this approach and the resulting measurement uncertainties have

not been assessed yet. Moreover, often, only values for a single *P* are given. Only recently, an increasing number of absolute Φ_{UC} measurements has been reported [102, 123, 126–130], with the highest Φ_{UC} values of Yb^{3+},Er^{3+}-based systems stated so far being 7.8% for a $NaYF_4$:Yb^{3+},Er^{3+} micrometer-sized $NaYF_4$:Yb^{3+},Er^{3+} powder at *P* of 22 W cm^{-2} [128], and 6.7% for 40-nm core–shell $LiLuF_4$:Yb^{3+},Er^{3+} particles at *P* of 127 W cm^{-2} [130]. Nevertheless, often a detailed description of the instrumentation and actual performance of the measurements is missing. To improve the reliability of Φ_{UC} data and determine typical uncertainties, interlaboratory comparisons of $\Phi_{UC}(P)$ measurements of representative UCNPs are required, with all participants measuring the same materials [131]. This could also be used to establish a set of spectroscopically well characterized UCNPs as quantum yield standards for quantitative UCL studies, thereby providing tools for establishing these techniques in different laboratories worldwide.

New spectroscopic trends: photoluminescence measurements beyond 1000 nm exploiting also the DC emission of NIR-excited Ln^{3+}-based nanoparticles

A current trend in fluorescence imaging is the use of optical reporters with emission in the so-called SWIR or second NIR (NIR-II) biological window from approximately 1000 to 1700 nm [132, 133]. Emission in the SWIR (sometimes ascribed to the wavelength region from 1000 to 1350 nm or 1400 nm) is better suited for deep tissue and high contrast optical imaging than emission in the NIR, yielding improved signals and improved resolution at all tissue depths, most likely owing to the reduced scattering of photons in this wavelength region. This minimizes image blurring. A very prominent example is the through-skull fluorescence imaging of the brain [134]. The future importance of this trend is underlined by recent reviews, where different NIR-emissive inorganic luminescent probes for the first diagnostic window (NIR or NIR-I, from approximately 650 to 950 nm) and the SWIR are summarized [135–138].

Ln^{3+}-based materials such as $NaYF_4$:Yb^{3+}/Ln^{3+}@$NaYF_4$ core–shell nanoparticles are also attractive reporters for this wavelength region, here exploiting not the NIR-excited nonlinear UCL of these UCNPs in the UV/visible/NIR but the linear DC or Stokes-shifted emission of certain Ln^{3+} ions downshifted to longer wavelength than the excitation. As shown in Fig. 9a, Ln^{3+} ions such as Yb^{3+}, Nd^{3+}, Pr^{3+}, Tm^{3+}, and Er^{3+} display emission bands above 1000 nm that are accessible either by direct excitation of the respective emissive Ln^{3+} ion (which, however, can have a very low absorption cross section) or by so-called NIR-to-SWIR UC resulting in the DC luminescence (DCL) of the Ln^{3+} ions [133]. The superior tissue transmission of the SWIR emission of Ln^{3+}-based materials (1525 nm) compared with conventionally used NIR emission (808 nm) follows from Fig. 9b [133]. The increasing interest in the SWIR wavelength region triggered the first comparisons of the luminescence properties and SWIR imaging potential of Ln^{3+}-based materials and, for example, SWIR-emissive semiconductor nanocrystals [135–138].

Principally, both UCL and DCL of Ln^{3+}-based UCNPs can be used for signaling, sensing, and imaging. Moreover, in principle, measurements of nonlinear UCL and linear DCL can be performed simultaneously, which allows imaging in a very broad spectral region. It has to be kept in mind, however, that an efficient DC emission may be counterproductive for a high UCL. A particularly elegant example of imaging in the SWIR with Ln^{3+}-based nanoparticles commonly used as UCNPs was recently reported by the Prasad group [139] with $NaYF_4$:Yb^{3+}/X^{3+}@$NaYbF_4$@$NaYF_4$:Nd^{3+} (X is no ion, Er^{3+}, Ho^{3+}, Tm^{3+}, or Pr^{3+}) nanocrystals, surface functionalized with the light-harvesting NIR dye indocyanine green (ICG). These nanoparticles produced a set of narrowband DC emissions with a large Stokes shift (more than 200 nm) in the SWIR by directional energy transfer from ICG, via Ln^{3+} ions in the shells, to the emitter X^{3+} in the core. These materials, which are excitable in the wavelength region from 700 to 860 nm, provide a better imaging profile than Yb^{3+}/Tm^{3+}-co-doped UCNPs imaged in the NIR region (termed also NIR-I), here from 700 to 950 nm [139].

A prerequisite for SWIR imaging with Ln^{3+}-based materials and other reporter candidates is in any case reliable quantitative spectroscopic studies in this still challenging wavelength region as underlined in the previous section for UCL measurements. The assessment and comparability of optical reporters for the SWIR is currently complicated by the lack of established calibration procedures and standards for this rather new wavelength region. For example, the rather large variabilities in fluorescence quantum yields in this spectral region was only recently demonstrated for SWIR-emissive dyes such as IR-26 and semiconductor quantum dots, yielding variations by factors of 5–10 [52, 140].

Conclusion and future directions

In summary, in recent years, the synthesis of UCNPs has matured with synthetic routes to sophisticated core–shell nanostructures with increasingly precise control of the dopant level and shell thickness emerging, which allows many interesting applications in the life and material sciences. The design of the next generation of UCNPs will focus on strategies that provide precise control over the size and crystal phase as well as dopant concentration and its local homogeneity and that allow tuning of the bandwidth and color for spectral alignment. Of increasing relevance will also be the reproducibility

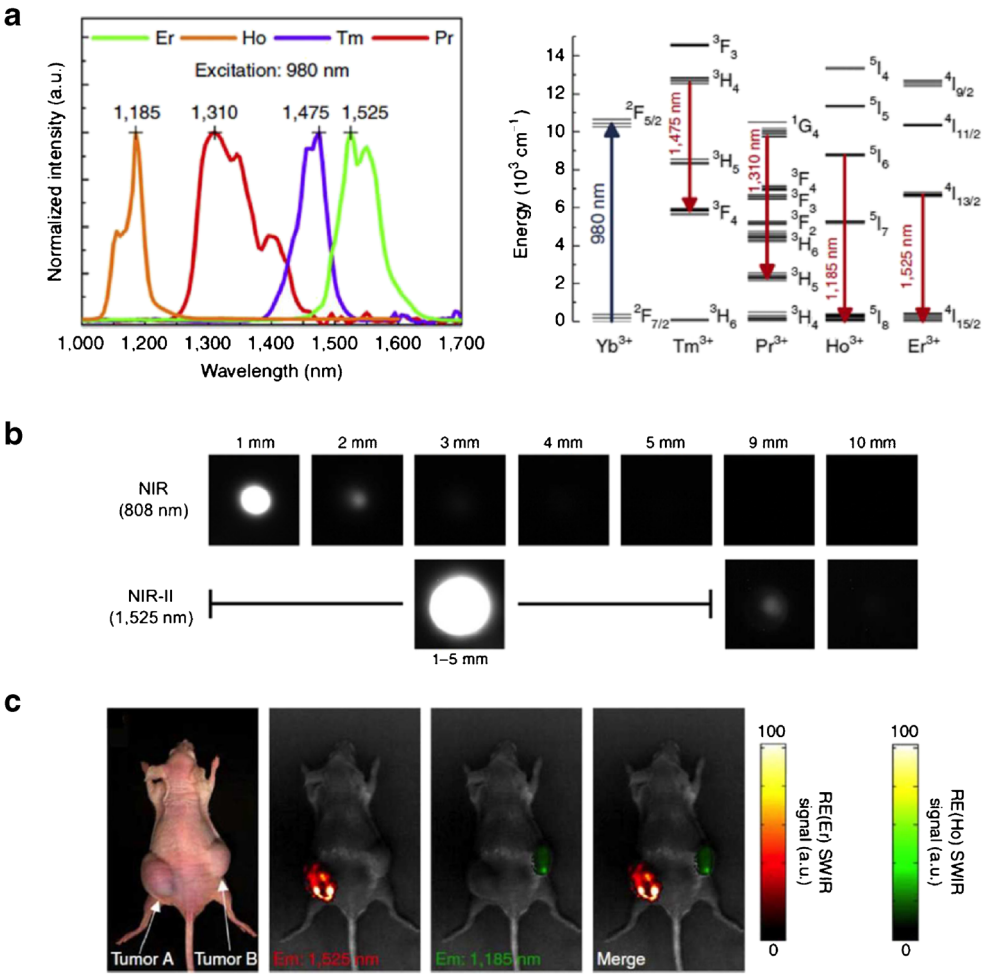

Fig. 9 $NaYF_4:Yb^{3+}/Ln^{3+}@NaYF_4$ core–shell nanoparticles (Ln^{3+} is Er^{3+}, Ho^{3+}, Tm^{3+}, or Pr^{3+}) as NIR-II or short-wavelength infrared (SWIR) reporters. **a** SWIR or NIR-II emission spectra and energy diagram of lanthanide-doped nanoparticles. **b** Comparison of the tissue transmission of SWIR or NIR-II emission (1525 nm) compared with NIR emission (808 nm). **c** Multispectral imaging of tumor using SWIR or NIR-II fluorescent reporters. (Reprinted with permission from [133])

and potential for upscaling for the preparation of large batches of high-quality UCNPs (core-only and core–shell nanostructures). As a general trend, the search for new and improved design concepts for UCNPs will be increasingly guided by quantitative spectroscopic studies of UCL and measurements of the UC quantum yield (Φ_{UC}) in different UC nanostructures as well as theoretical simulations of the energy transfer mechanism in these UC materials. In particular, the design of new core–shell nanoparticles will be explored to improve the low brightness of existing UCNPs. Additional strategies such as plasmonic enhancement or the recently reported magnetic field modulation of UCNPs [140] may also play a role. In this respect, protocols for the determination of particularly relevant performance parameters such as Φ_{UC} will be required to pave the way for a standardized comparison of UC nanomaterials and enhancement concepts. An example is the recently reported protocol for the relative and absolute determination of fluorescence quantum yields of nonscattering solutions of dyes and colloidal quantum dots [121]. Moreover, analytical tools and protocols for the characterization of UCNPs need to be better standardized as is currently being done for other nanomaterials as well [148]. Because of doping with different Ln^{3+} ions and the importance of the spatial distribution of the different sensitizer and activator ions, this presents a particular challenge. Moreover, the tailoring of UCNPs for specific applications regarding laser power density P (low P of about 10 W cm^{-2} as used, e.g., in assays; standard imaging and spectroscopy applications with P of about 10–100 W cm^{-2} and high $P > 10^5$ W cm^{-2} as used for single-particle studies) and surface modification is important for optimum material performance. In this respect, it could also be mandatory to revisit optimum dopant concentrations for different UC host materials, UCNP sizes, and environments/applications. This could be addressed, for example, with UCNP libraries that allow fast screening of suitable dopant concentrations and dopant ratios under application-relevant conditions as recently shown by Chan [149].

For the broad use of UC (nano)technology, commercial instrumentation for different types of UC measurements/applications will be required. Currently, commercial instrumentation for the readout of UCNPs is very limited, and most research groups around the world use custom-built instrumentation for their measurements, which is often not well characterized, for example, with respect to the beam profile and laser

power density reaching the sample. Hamamatsu developed a first prototype of an integrating sphere setup equipped with a 980-nm laser diode for absolute measurements of UCL and Φ_{UC}.

In support of these developments and needs, COST Action CM1403 "The European Upconversion Network: From the Design of Photon-Upconverting Nanomaterials to Biomedical Applications" was established. The goal of COST Action CM1403 is to address many of these challenges of UC technology highlighted in this review series. This ranges from the reproducible and upscalable preparation of high-quality UCNPs and the development of spectroscopic characterization tools with particular focus on absolute measurements of *P*-dependent UCL and Φ_{UC} for the quantification of luminescence quenching channels and protocols for surface functionalization to applications in fluorescence assays, bioimaging studies, and sensor materials in a multidisciplinary approach.

Acknowledgements Financial support from the German Research Foundation (grants RE 1203/18-1, RE 1203/20-1, GO 1968/5-1, and GO 1968/6-1) and COST Action CM1403 "The European Upconversion Network: From the Design of Photon-Upconverting Nanomaterials to Biomedical Applications" is gratefully acknowledged.

Compliance with ethical standards

Conflict of interest The authors declare that they have no conflict of interest.

References

1. Zhu XJ, Su QQ, Feng W, Li FY. Anti-Stokes shift luminescent materials for bio-applications. Chem Soc Rev. 2017;46(4):1025–39. doi:10.1039/c6cs00415f.
2. Nadort A, Zhao JB, Goldys EM. Lanthanide upconversion luminescence at the nanoscale: fundamentals and optical properties. Nanoscale. 2016;8(27):13099–130. doi:10.1039/c5nr08477f.
3. Gai SL, Li CX, Yang PP, Lin J. Recent progress in rare earth micro/nanocrystals: soft chemical synthesis, luminescent properties, and biomedical applications. Chem Rev. 2014;114(4):2343–89. doi:10.1021/cr4001594.
4. Wu X, Chen GY, Shen J, Li ZJ, Zhang YW, Han G. Upconversion nanoparticles: a versatile solution to multiscale biological imaging. Bioconjugate Chem. 2015;26(2):166–75. doi:10.1021/bc5003967.
5. Xu CT, Zhan QQ, Liu HC, Somesfalean G, Qian J, He SL, et al. Upconverting nanoparticles for pre-clinical diffuse optical imaging, microscopy and sensing: current trends and future challenges. Laser Photon Rev. 2013;7(5):663–97. doi:10.1002/lpor.201200052.
6. Wang HQ, Batentschuk M, Osvet A, Pinna L, Brabec CJ. Rare-earth ion doped up-conversion materials for photovoltaic applications. Adv Mater. 2011;23(22-23):2675–80. doi:10.1002/adma.201100511.
7. Gnach A, Bednarkiewicz A. Lanthanide-doped up-converting nanoparticles: merits and challenges. Nano Today. 2012;7(6):532–63. doi:10.1016/j.nantod.2012.10.006.
8. Wang F, Liu XG. Recent advances in the chemistry of lanthanide-doped upconversion nanocrystals. Chem Soc Rev. 2009;38(4):976–89. doi:10.1039/b809132n.
9. Goldschmidt JC, Fischer S. Upconversion for photovoltaics - a review of materials, devices and concepts for performance enhancement. Adv Opt Mater. 2015;3(4):510–35. doi:10.1002/adom.201500024.
10. Zheng W, Huang P, Tu D, Ma E, Zhu H, Chen X. Lanthanide-doped upconversion nano-bioprobes: electronic structures, optical properties, and biodetection. Chem Soc Rev. 2015;44(6):1379–415. doi:10.1039/c4cs00178h.
11. Zhou J, Liu Q, Feng W, Sun Y, Li F. Upconversion luminescent materials: advances and applications. Chem Rev. 2015;115(1):395–465. doi:10.1021/cr400478f.
12. Zhou B, Shi B, Jin D, Liu X. Controlling upconversion nanocrystals for emerging applications. Nat Nano. 2015;10(11):924–36. doi:10.1038/nnano.2015.251.
13. Gorris HH, Wolfbeis OS. Photon-upconverting nanoparticles for optical encoding and multiplexing of cells, biomolecules, and microspheres. Angew Chem Int Ed. 2013;52(13):3584–600. doi:10.1002/anie.201208196.
14. Hyppanen I, Lahtinen S, Aaritalo T, Makela J, Kankare J, Soukka T. Photon upconversion in a molecular lanthanide complex in anhydrous solution at room temperature. ACS Photon. 2014;1(5):394–7. doi:10.1021/ph500047j.
15. Nonat A, Chan CF, Liu T, Platas-Iglesias C, Liu ZY, Wong WT, et al. Room temperature molecular up conversion in solution. Nat Commun. 2016;7:11978. doi:10.1038/ncomms11978.
16. Souri N, Tian PP, Platas-Iglesias C, Wong KL, Nonat A, Charbonniere LJ. Upconverted photosensitization of Tb visible emission by NIR Yb excitation in discrete supramolecular heteropolynuclear complexes. J Am Chem Soc. 2017;139(4):1456–9. doi:10.1021/jacs.6b12940.
17. Aboshyan-Sorgho L, Cantuel M, Petoud S, Hauser A, Piguet C. Optical sensitization and upconversion in discrete polynuclear chromium-lanthanide complexes. Coord Chem Rev. 2012;256(15-16):1644–63. doi:10.1016/j.ccr.2011.12.013.
18. Auzel F. Upconversion and anti-stokes processes with f and d ions in solids. Chem Rev. 2004;104(1):139–73. doi:10.1021/cr020357g.
19. Haase M, Schäfer H. Upconverting nanoparticles. Angew Chem Int Ed. 2011;50(26):5808–29. doi:10.1002/anie.201005159.
20. Chan EM, Levy ES, Cohen BE. Rationally designed energy transfer in upconverting nanoparticles. Adv Mater. 2015;27(38):5753–61. doi:10.1002/adma.201500248.
21. Anderson RB, Smith SJ, May PS, Berry MT. Revisiting the NIR-to-visible upconversion mechanism in β-NaYF4:Yb3+, Er3+. J Phys Chem Lett. 2014;5(1):36–42. doi:10.1021/jz402366r.
22. Berry MT, May PS. Disputed mechanism for NIR-to-red upconversion luminescence in NaYF4:Yb3+, Er3+. J Phys Chem A. 2015;119(38):9805–11. doi:10.1021/acs.jpca.5b08324.
23. Pichaandi J, Boyer JC, Delaney KR, van Veggel F. Two-photon upconversion laser (scanning and wide-field) microscopy Using Ln^{3+}-doped $NaYF_4$ upconverting nanocrystals: a critical evaluation of their performance and potential in bioimaging. J Phys Chem C. 2011;115(39):19054–64. doi:10.1021/jp206345j.
24. Dong H, Du SR, Zheng XY, Lyu GM, Sun LD, Li LD, et al. Lanthanide nanoparticles: From design toward bioimaging and therapy. Chem Rev. 2015;115(19):10725–815. doi:10.1021/acs.chemrev.5b00091.
25. Hao SW, Chen GY, Yang CH. Sensing using rare-earth-doped upconversion nanoparticles. Theranostics. 2013;3(5):331–45. doi:10.7150/thno.5305.
26. Sedlmeier A, Gorris HH. Surface modification and characterization of photon-upconverting nanoparticles for bioanalytical

applications. Chem Soc Rev. 2015;44(6):1526–60. doi:10.1039/c4cs00186a.
27. Wolfbeis OS. An overview of nanoparticles commonly used in fluorescent bioimaging. Chem Soc Rev. 2015;44(14):4743–68. doi:10.1039/c4cs00392f.
28. Mader HS, Kele P, Saleh SM, Wolfbeis OS. Upconverting luminescent nanoparticles for use in bioconjugation and bioimaging. Curr Opin Chem Biol. 2010;14:1–15. doi:10.1016/j.cbpa.2010.08.014.
29. Liu YS, Tu DT, Zhu HM, Chen XY. Lanthanide-doped luminescent nanoprobes: controlled synthesis, optical spectroscopy, and bioapplications. Chem Soc Rev. 2013;42(16):6924–58. doi:10.1039/C3cs60060b.
30. Zhou AG, Wei YC, Chen Q, Xing D. In vivo near-infrared photodynamic therapy based on targeted upconversion nanoparticles. J Biomed Nanotechnol. 2015;11(11):2003–10. doi:10.1166/jbn.2015.2150.
31. Zou XM, Liu Y, Zhu XJ, Chen M, Yao LM, Feng W, et al. An Nd^{3+}-sensitized upconversion nanophosphor modified with a cyanine dye for the ratiometric upconversion luminescence bioimaging of hypochlorite. Nanoscale. 2015;7(9):4105–13. doi:10.1039/c4nr06407k.
32. Wang X, Yang CX, Chen JT, Yan XP. A dual-targeting upconversion nanoplatform for two-color fluorescence imaging-guided photodynamic therapy. Anal Chem. 2014;86(7):3263–7. doi:10.1021/ac500060c.
33. Zhang X, Tian G, Yin WY, Wang LM, Zheng XP, Yan L, et al. Controllable generation of nitric oxide by near-infrared-sensitized upconversion nanoparticles for tumor therapy. Adv Funct Mater. 2015;25(20):3049–56. doi:10.1002/adfm.201404402.
34. Rodriguez-Sevilla P, Rodriguez-Rodriguez H, Pedroni M, Speghini A, Bettinelli M, Sole JG, et al. Assessing single upconverting nanoparticle luminescence by optical tweezers. Nano Lett. 2015;15(8):5068–74. doi:10.1021/acs.nanolett.5b01184.
35. Rodriguez-Sevilla P, Labrador-Paez L, Wawrzynczyk D, Nyk M, Samoc M, Kar AK, et al. Determining the 3D orientation of optically trapped upconverting nanorods by in situ single-particle polarized spectroscopy. Nanoscale. 2016;8(1):300–8. doi:10.1039/c5nr06419h.
36. van der Ende BM, Aarts L, Meijerink A. Lanthanide ions as spectral converters for solar cells. Phys Chem Chem Phys. 2009;11(47):11081–95. doi:10.1039/b913877c.
37. Yuan CZ, Chen GY, Li L, Damasco JA, Ning ZJ, Xing H, et al. Simultaneous multiple wavelength upconversion in a core-shell nanoparticle for enhanced near infrared light harvesting in a dye-sensitized solar cell. ACS Appl Mater Interfaces. 2014;6(20):18018–25. doi:10.1021/am504866g.
38. Zheng W, Zhou SY, Chen Z, Hu P, Liu YS, Tu DT, et al. Sub-10nm lanthanide-doped CaF_2 nanoprobes for time-resolved luminescent biodetection. Angew Chem Int Ed. 2013;52(26):6671–6. doi:10.1002/anie.201302481.
39. Baride A, Meruga JM, Douma C, Langerman D, Crawford G, Kellar JJ, et al. A NIR-to-NIR upconversion luminescence system for security printing applications. RSC Adv. 2015;5(123):101338–46. doi:10.1039/c5ra20785a.
40. Qiu PY, Zhou N, Chen HY, Zhang CL, Gao G, Cui DX. Recent advances in lanthanide-doped upconversion nanomaterials: synthesis, nanostructures and surface modification. Nanoscale. 2013;5(23):11512–25. doi:10.1039/c3nr03642a.
41. Noculak A, Podhorodecki A, Pawlik G, Banski M, Misiewicz J. Ion-ion interactions in β-$NaGdF_4$:Yb^{3+}, Er^{3+} nanocrystals - the effect of ion concentration and their clustering. Nanoscale. 2015;7(32):13784–92. doi:10.1039/c5nr03385c.
42. Gainer CF, Romanowski M. A review of synthetic methods for the production of upconverting lanthanide nanoparticles. J Innov Opt Health Sci. 2014;7(2):1330007. doi:10.1142/s1793545813300073.
43. Lin M, Zhao Y, Wang SQ, Liu M, Duan ZF, Chen YM, et al. Recent advances in synthesis and surface modification of lanthanide-doped upconversion nanoparticles for biomedical applications. Biotechnol Adv. 2012;30(6):1551–61. doi:10.1016/j.biotechadv.2012.04.009.
44. Wang F, Deng R, Liu X. Preparation of core-shell $NaGdF_4$ nanoparticles doped with luminescent lanthanide ions to be used as upconversion-based probes. Nat Protoc. 2014;9(7):1634–44. doi:10.1038/nprot.2014.111.
45. Wilhelm S, Kaiser M, Würth C, Heiland J, Carrillo-Carrion C, Muhr V, et al. Water dispersible upconverting nanoparticles: effects of surface modification on their luminescence and colloidal stability. Nanoscale. 2015;7(4):1403–10. doi:10.1039/C4nr05954a.
46. Rinkel T, Raj AN, Duhnen S, Haase M. Synthesis of 10nm-NaYF4:Yb, Er/NaYF4 core/shell upconversion nanocrystals with 5nm particle cores. Angew Chem Int Ed. 2016;55(3):1164–7. doi:10.1002/anie.201508838.
47. Chen GY, Agren H, Ohulchanskyy TY, Prasad PN. Light upconverting core-shell nanostructures: nanophotonic control for emerging applications. Chem Soc Rev. 2015;44(6):1680–713. doi:10.1039/c4cs00170b.
48. Duhnen S, Haase M. Study on the intermixing of core and shell in $NaEuF_4$/$NaGdF_4$ core/shell nanocrystals. Chem Mater. 2015;27(24):8375–86. doi:10.1021/acs.chemmater.5b03846.
49. Li XM, Shen DK, Yang JP, Yao C, Che RC, Zhang F, et al. Successive layer-by-layer strategy for multi-shell epitaxial growth: shell thickness and doping position dependence in upconverting optical properties. Chem Mater. 2013;25(1):106–12. doi:10.1021/cm3033498.
50. Li XM, Wang R, Zhang F, Zhao DY. Engineering homogeneous doping in single nanoparticle to enhance upconversion efficiency. Nano Lett. 2014;14(6):3634–9. doi:10.1021/nl501366x.
51. Huber A, Behnke T, Würth C, Jaeger C, Resch-Genger U. Spectroscopic characterization of coumarin-stained beads: quantification of the number of fluorophores per particle with solid-state ^{19}F-NMR and measurement of absolute fluorescence quantum yields. Anal Chem. 2012;84(8):3654–61. doi:10.1021/ac3000682.
52. Würth C, Geißler D, Behnke T, Kaiser M, Resch-Genger U. Critical review of the determination of photoluminescence quantum yields of luminescent reporters. Anal Bioanal Chem. 2015;407(1):59–78. doi:10.1007/s00216-014-8130-z.
53. Ye S, Chen GY, Shao W, Qu JL, Prasad PN. Tuning upconversion through a sensitizer/activator-isolated $NaYF_4$ core/shell structure. Nanoscale. 2015;7(9):3976–84. doi:10.1039/c4nr07678h.
54. Lu J, Chen YH, Liu DM, Ren W, Lu YQ, Shi Y, et al. One-step protein conjugation to upconversion nanoparticles. Anal Chem. 2015;87(20):10406–13. doi:10.1021/acs.analchem.5b02523.
55. Wang F, Han Y, Lim CS, Lu YH, Wang J, Xu J, et al. Simultaneous phase and size control of upconversion nanocrystals through lanthanide doping. Nature. 2010;463(7284):1061–5. doi:10.1038/nature08777.
56. Vetrone F, Naccache R, Mahalingam V, Morgan CG, Capobianco JA. The active-core/active-shell approach: a strategy to enhance the upconversion luminescence in lanthanide-doped nanoparticles. Adv Funct Mater. 2009;19(18):2924–9. doi:10.1002/adfm.200900234.
57. Wang Y, Liu K, Liu XM, Dohnalova K, Gregorkiewicz T, Kong XG, et al. Critical shell thickness of core/shell upconversion luminescence nanoplatform for FRET application. J Phys Chem Lett. 2011;2(17):2083–8. doi:10.1021/jz200922f.
58. Wei W, Zhang Y, Chen R, Goggi J, Ren N, Huang L, et al. Cross relaxation induced pure red upconversion in activator- and

sensitizer-rich lanthanide nanoparticles. Chem Mater. 2014;26(18):5183–6. doi:10.1021/cm5022382.

59. Boyer JC, Manseau MP, Murray JI, van Veggel F. Surface modification of upconverting $NaYF_4$ manoparticles with PEG-phosphate ligands for NIR (800 nm) biolabeling within the biological window. Langmuir. 2010;26(2):1157–64. doi:10.1021/la902260j.
60. Wawrzynczyk D, Bednarkiewicz A, Nyk M, Cichos J, Karbowiak M, Hreniak D, et al. Optimisation of ligand exchange towards stable water suspensions of crystalline $NaYF_4$:Er^{3+}, Yb^{3+} nanoluminophors. J Nanosci Nanotechnol. 2012;12(3):1886–91. doi:10.1166/jnn.2012.5202.
61. Shen J, Chen GY, Vu AM, Fan W, Bilsel OS, Chang CC, et al. Engineering the upconversion nanoparticle excitation wavelength: cascade sensitization of tri-doped upconversion colloidal nanoparticles at 800 nm. Adv Opt Mater. 2013;1(9):644–50. doi:10.1002/adom.201300160.
62. Han SY, Deng RR, Xie XJ, Liu XG. Enhancing luminescence in lanthanide-doped upconversion nanoparticles. Angew Chem Int Ed. 2014;53(44):11702–15. doi:10.1002/anie.201403408.
63. Fischer S, Johnson NJJ, Pichaandi J, Goldschmidt JC, van Veggel FCJM. Upconverting core-shell nanocrystals with high quantum yield under low irradiance: on the role of isotropic and thick shells. J Appl Phys. 2015;118(19):193105. doi:10.1063/1.4936119.
64. Xue XJ, Uechi S, Tiwari RN, Duan ZC, Liao MS, Yoshimura M, et al. Size-dependent upconversion luminescence and quenching mechanism of $LiYF_4$: Er^{3+}/Yb^{3+} nanocrystals with oleate ligand adsorbed. Opt Mater Express. 2013;3(7):989–99. doi:10.1364/ome.3.000989.
65. Arppe R, Hyppanen I, Perala N, Peltomaa R, Kaiser M, Wurth C, et al. Quenching of the upconversion luminescence of NaYF4: Yb3+, Er3+ and NaYF4:Yb3+, Tm3+ nanophosphors by water: the role of the sensitizer Yb3+ in non-radiative relaxation. Nanoscale. 2015;7(27):11746–57. doi:10.1039/c5nr02100f.
66. Klier DT, Kumke MU. Analysing the effect of the crystal structure on upconversion luminescence in Yb^{3+}, Er^{3+}-co-doped $NaYF_4$ nanomaterials. J Mater Chem C. 2015;3(42):11228–38. doi:10.1039/c5tc02218e.
67. Zhang F, Che R, Li X, Yao C, Yang J, Shen D, et al. Direct imaging the upconversion nanocrystal core/shell structure at the subnanometer level: shell thickness dependence in upconverting optical properties. Nano Lett. 2012;12(6):2852–8. doi:10.1021/nl300421n.
68. Qiu HL, Yang CH, Shao W, Damasco J, Wang XL, Agren H, et al. Enhanced upconversion luminescence in Yb^{3+}/Tm^{3+}-codoped fluoride active core/active shell/inert shell nanoparticles through directed energy migration. Nanomaterials. 2014;4(1):55–68. doi:10.3390/nano4010055.
69. Kar A, Patra A. Impacts of core-shell structures on properties of lanthanide-based nanocrystals: crystal phase, lattice strain, downconversion, upconversion and energy transfer. Nanoscale. 2012;4(12):3608–19. doi:10.1039/c2nr30389b.
70. Fischer S, Bronstein ND, Swabeck JK, Chan EM, Alivisatos AP. Precise tuning of surface quenching for luminescence enhancement in core–shell lanthanide-doped nanocrystals. Nano Lett. 2016;16(11):7241–7. doi:10.1021/acs.nanolett.6b03683.
71. Wang F, Deng RR, Wang J, Wang QX, Han Y, Zhu HM, et al. Tuning upconversion through energy migration in core-shell nanoparticles. Nat Mater. 2011;10(12):968–73. doi:10.1038/nmat3149.
72. Dong H, Sun LD, Wang YF, Ke J, Si R, Xiao JW, et al. Efficient tailoring of upconversion selectivity by engineering local structure of lanthanides in Na_xREF^{3+x} nanocrystals. J Am Chem Soc. 2015;137(20):6569–76. doi:10.1021/jacs.5b01718.
73. Cheng Q, Sui JH, Cai W. Enhanced upconversion emission in Yb^{3+} and Er^{3+} codoped $NaGdF_4$ nanocrystals by introducing Li^+ ions. Nanoscale. 2012;4(3):779–84. doi:10.1039/c1nr11365h.
74. Kim JH, Choi H, Kim EO, Noh HM, Moon BK, Jeong JH. Li doping effects on the upconversion luminescence of Yb^{3+}/Er^{3+}-doped ABO_4 (A = Ca, Sr; B = W, Mo) phosphors. Opt Mater. 2014;38:113–8. doi:10.1016/j.optmat.2014.09.035.
75. Ding MY, Ni YR, Song Y, Liu XX, Cui TL, Chen DQ, et al. Li^+ ions doping core-shell nanostructures: an approach to significantly enhance upconversion luminescence of lanthanide-doped nanocrystals. J Alloys Compd. 2015;623:42–8. doi:10.1016/j.jallcom.2014.10.089.
76. Tang J, Chen L, Li J, Wang Z, Zhang JH, Zhang LG, et al. Selectively enhanced red upconversion luminescence and phase/size manipulation via $Fe3^+$ doping in $NaYF_4$:Yb, Er nanocrystals. Nanoscale. 2015;7(35):14752–9. doi:10.1039/c5nr04125b.
77. Wang C, Cheng L, Liu YM, Wang XJ, Ma XX, Deng ZY, et al. Imaging-guided pH-sensitive photodynamic therapy using charge reversible upconversion nanoparticles under near-infrared light. Adv Funct Mater. 2013;23(24):3077–86. doi:10.1002/adfm.201202992.
78. Wu ZN, Lin M, Liang S, Liu Y, Zhang H, Yang B. Hot-injection synthesis of manganese-ion-doped NaYF4:Yb, Er nanocrystals with red up-converting emission and tunable diameter. Part Part Syst Charact. 2013;30(4):311–5. doi:10.1002/ppsc.201200106.
79. Resch-Genger U, Grabolle M, Cavaliere-Jaricot S, Nitschke R, Nann T. Quantum dots versus organic dyes as fluorescent labels. Nat Methods. 2008;5(9):763–75.
80. Chen GY, Ohulchanskyy TY, Kumar R, Agren H, Prasad PN. Ultrasmall monodisperse $NaYF_4$:Yb^{3+}/Tm^{3+} Nanocrystals with enhanced near-infrared to near-infrared upconversion photoluminescence. ACS Nano. 2010;4(6):3163–8. doi:10.1021/nn100457j.
81. Noculak A, Fhui YS, Banski M, Misiewicz J, Podhorodecki A (2014) Yb^{3+} and Tm^{3+} concentration-dependent structural and optical properties of hexagonal $NaGdF_4$ nanocrystals. J Nanoparticle Res 16(5). doi:10.1007/s11051-014-2396-0.
82. Xu DK, Liu CF, Yan JW, Yang SH, Zhang YL. Understanding energy transfer mechanisms for tunable emission of $Yb^{3+}Er^{3+}$ codoped GdF_3 nanoparticles: concentration-dependent luminescence by near-infrared and violet excitation. J Phys Chem C. 2015;119(12):6852–60. doi:10.1021/acs.jpcc.5b00882.
83. Zhan QQ, Qian J, Liang HJ, Somesfalean G, Wang D, He SL, et al. Using 915 nm laser excited Tm^{3+}/Er^{3+}/Ho^{3+}-doped $NaYbF_4$ upconversion nanoparticles for in vitro and deeper in vivo bioimaging without overheating irradiation. ACS Nano. 2011;5(5):3744–57. doi:10.1021/nn200110j.
84. Wang YF, Liu GY, Sun LD, Xiao JW, Zhou JC, Yan CH. Nd^{3+}-sensitized upconversion nanophosphors: efficient in vivo bioimaging probes with minimized heating effect. ACS Nano. 2013;7(8):7200–6. doi:10.1021/nn402601d.
85. Xie XJ, Gao NY, Deng RR, Sun Q, Xu QH, Liu XG. Mechanistic investigation of photon upconversion in Nd^{3+}-sensitized core-shell nanoparticles. J Am Chem Soc. 2013;135(34):12608–11. doi:10.1021/ja4075002.
86. Pokhrel M, Mimun LC, Yust B, Kumar GA, Dhanale A, Tang L, et al. Stokes emission in GdF_3:Nd^{3+} nanoparticles for bioimaging probes. Nanoscale. 2014;6(3):1667–74. doi:10.1039/c3nr03317a.
87. del Rosal B, Perez-Delgado A, Misiak M, Bednarkiewicz A, Vanetsev AS, Orlovskii Y, et al. Neodymium-doped nanoparticles for infrared fluorescence bioimaging: the role of the host. J Appl Phys. 2015;118(14):143104. doi:10.1063/1.4932669.
88. Rocha U, Jacinto C, Silva WF, Guedes I, Benayas A, Maestro LM, et al. Subtissue thermal sensing based on neodymium-doped LaF_3 nanoparticles. ACS Nano. 2013;7(2):1188–99. doi:10.1021/nn304373q.

89. Huang XY, Lin J. Active-core/active-shell nanostructured design: an effective strategy to enhance Nd^{3+}/Yb^{3+} cascade sensitized upconversion luminescence in lanthanide-doped nanoparticles. J Mater Chem C. 2015;3(29):7652–7. doi:10.1039/c5tc01438g.
90. Zou WQ, Visser C, Maduro JA, Pshenichnikov MS, Hummelen JC. Broadband dye-sensitized upconversion of near-infrared light. Nat Photon. 2012;6(8):560–4. doi:10.1038/nphoton.2012.158.
91. Chen G, Shao W, Valiev RR, Ohulchanskyy TY, He GS, Ågren H, et al. Efficient broadband upconversion of near-infrared light in dye-sensitized core/shell nanocrystals. Adv Opt Mater. 2016;4(11):1760–6. doi:10.1002/adom.201600556.
92. Wu X, Lee H, Bilsel O, Zhang YW, Li ZJ, Chen T, et al. Tailoring dye-sensitized upconversion nanoparticle excitation bands towards excitation wavelength selective imaging. Nanoscale. 2015;7(44):18424–8. doi:10.1039/c5nr05437k.
93. Wu X, Zhang YW, Takle K, Bilsel O, Li ZJ, Lee H, et al. Dye-sensitized core/active shell upconversion nanoparticles for optogenetics and bioimaging applications. ACS Nano. 2016;10(1):1060–6. doi:10.1021/acsnano.5b06383.
94. Muhr V, Würth C, Kraft M, Buchner M, Baeumner AJ, Resch-Genger U, et al. Particle-size-dependent Förster resonance energy transfer from upconversion nanoparticles to organic dyes. Anal Chem. 2017;89(9):4868–74. doi:10.1021/acs.analchem.6b04662.
95. Hildebrandt N, Spillmann CM, Algar WR, Pons T, Stewart MH, Oh E, et al. Energy transfer with semiconductor quantum dot bioconjugates: a versatile platform for biosensing, energy harvesting, and other developing applications. Chem Rev. 2017;117(2):536–711. doi:10.1021/acs.chemrev.6b00030.
96. Chen GY, Shen J, Ohulchanskyy TY, Patel NJ, Kutikov A, Li ZP, et al. (α-$NaYbF_4$:Tm^{3+})/CaF_2 core/shell nanoparticles with efficient near-infrared to near-infrared upconversion for high-contrast deep tissue bioimaging. ACS Nano. 2012;6(9):8280–7. doi:10.1021/nn302972r.
97. Riuttamäki T, Soukka T. Upconverting phosphor labels for bioanalytical assays. In: Matysik F-M, editor. Advances in chemical bioanalysis. Cham: Springer; 2013. p. 155–204. doi:10.1007/11663_2013_3.
98. Pakkila H, Yliharsila M, Lahtinen S, Hattara L, Salminen N, Arppe R, et al. Quantitative multianalyte microarray immunoassay utilizing upconverting phosphor technology. Anal Chem. 2012;84(20):8628–34. doi:10.1021/ac301719p.
99. Wurth C, Kaiser M, Wilhelm S, Grauel B, Hirsch T, Resch-Genger U. Excitation power dependent population pathways and absolute quantum yields of upconversion nanoparticles in different solvents. Nanoscale. 2017;9(12):4283–94. doi:10.1039/C7NR00092H.
100. Zhao JB, Jin DY, Schartner EP, Lu YQ, Liu YJ, Zvyagin AV, et al. Single-nanocrystal sensitivity achieved by enhanced upconversion luminescence. Nat Nanotechnol. 2013;8(10):729–34. doi:10.1038/nnano.2013.171.
101. Zhou JJ, Chen GX, Zhu YB, Huo LL, Mao W, Zou DN, et al. Intense multiphoton upconversion of Yb^{3+}-Tm^{3+} doped β-$NaYF_4$ individual nanocrystals by saturation excitation. J Mater Chem C. 2015;3(2):364–9. doi:10.1039/c4tc02363c.
102. Gargas DJ, Chan EM, Ostrowski AD, Aloni S, Altoe MVP, Barnard ES, et al. Engineering bright sub-10-nm upconverting nanocrystals for single-molecule imaging. Nat Nanotechnol. 2014;9(4):300–5. doi:10.1038/nnano.2014.29.
103. Gainer CF, Joshua GS, De Silva CR, Romanowski M. Control of green and red upconversion in NaYF4:Yb3+, Er3+ nanoparticles by excitation modulation. J Mater Chem. 2011;21(46):18530–3. doi:10.1039/c1jm13684d.
104. Liu Y, Lu Y, Yang X, Zheng X, Wen S, Wang F, et al. Amplified stimulated emission in upconversion nanoparticles for super-resolution nanoscopy. Nature. 2017;543(7644):229–33. doi:10.1038/nature21366.
105. Wang Y, Deng RR, Xie XJ, Huang L, Liu XG. Nonlinear spectral and lifetime management in upconversion nanoparticles by controlling energy distribution. Nanoscale. 2016;8(12):6666–73. doi:10.1039/c6nr00812g.
106. Chen P, Yu SL, Xu BB, Wang JC, Sang XW, Liu XF, et al. Enhanced upconversion luminescence in $NaYN_4$:Er nanoparticles with multi-wavelength excitation. Mater Lett. 2014;128:299–302. doi:10.1016/j.matlet.2014.04.179.
107. Wu DM, Garcia-Etxarri A, Salleo A, Dionne JA. Plasmon-enhanced upconversion. J Phys Chem Lett. 2014;5(22):4020–31. doi:10.1021/jz5019042.
108. Park W, Lu DW, Ahn SM. Plasmon enhancement of luminescence upconversion. Chem Soc Rev. 2015;44(10):2940–62. doi:10.1039/c5cs00050e.
109. Saboktakin M, Ye XC, Oh SJ, Hong SH, Fafarman AT, Chettiar UK, et al. Metal-enhanced upconversion luminescence tunable through metal nanoparticle-nanophosphor separation. ACS Nano. 2012;6(10):8758–66. doi:10.1021/nn302466r.
110. Xu W, Song HW, Chen X, Wang HY, Cui SB, Zhou DL, et al. Upconversion luminescence enhancement of Yb^{3+}, Nd^{3+} sensitized $NaYF_4$ core-shell nanocrystals on Ag grating films. Chem Commun. 2015;51(8):1502–5. doi:10.1039/c4cc08955c.
111. Xu W, Min XL, Chen X, Zhu YS, Zhou PW, Cui SB, et al. Ag-SiO_2-Er_2O_3 nanocomposites: highly effective upconversion luminescence at high power excitation and high temperature. Sci Rep. 2014;4:5087. doi:10.1038/srep05087.
112. Luo Q, Chen YR, Li ZQ, Zhu F, Chen XH, Sun Z, Wei YL, Guo H, Wang ZB, Huang SM (2014) Large enhancements of $NaYF_4$: Yb/Er/Gd nanorod upconversion emissions via coupling with localized surface plasmon of Au film. Nanotechnology 25(18). doi:10.1088/0957-4484/25/18/185401.
113. Niu XJ, Chen HY, Wang YQ, Wang WH, Sun XY, Chen LX. Upconversion fluorescence-SERS dual-mode tags for cellular and in vivo imaging. ACS Appl Mater Interfaces. 2014;6(7):5152–60. doi:10.1021/am500411m.
114. Li ZQ, Chen S, Li JJ, Liu QQ, Sun Z, Wang ZB, et al. Plasmon-enhanced upconversion fluorescence in NaYF4:Yb/Er/Gd nanorods coated with Au nanoparticles or nanoshells. J Appl Phys. 2012;111(1), 014310. doi:10.1063/1.3676258.
115. Green K, Wirth J, Lim SF. Optical investigation of gold shell enhanced 25 nm diameter upconverted fluorescence emission. Nanotechnology. 2016;27(13):135201. doi:10.1088/0957-4484/27/13/135201.
116. Feng AL, You ML, Tian LM, Singamaneni S, Liu M, Duan ZF, et al. Distance-dependent plasmon-enhanced fluorescence of upconversion nanoparticles using polyelectrolyte multilayers as tunable spacers. Sci Rep. 2015;5:7779. doi:10.1038/srep07779.
117. Fischer S, Kumar D, Hallermann F, von Plessen G, Goldschmidt JC. Enhanced upconversion quantum yield near spherical gold nanoparticles - a comprehensive simulation based analysis. Opt Express. 2016;24(6):A460–75. doi:10.1364/oe.24.00a460.
118. Kaiser M, Wurth C, Kraft M, Hyppanen I, Soukka T, Resch-Genger U. Power-dependent upconversion quantum yield of NaYF4:Yb3+, Er3+ nano- and micrometer-sized particles - measurements and simulations. Nanoscale. 2017. doi:10.1039/C7NR02449E.
119. Würth C, Grabolle M, Pauli J, Spieles M, Resch-Genger U. Relative and absolute determination of fluorescence quantum yields of transparent samples. Nat Protoc. 2013;8(8):1535–50. doi:10.1038/nprot.2013.087.
120. Wurth C, Resch-Genger U. Determination of photoluminescence quantum yields of scattering media with an integrating sphere: direct and indirect illumination. Appl Spectrosc. 2015;69(6):749–59. doi:10.1366/14-07679.

121. Boyer JC, van Veggel F. Absolute quantum yield measurements of colloidal $NaYF_4$: Er^{3+}, Yb^{3+} upconverting nanoparticles. Nanoscale. 2010;2(8):1417–9. doi:10.1039/c0nr00253d.
122. Xu CT, Svenmarker P, Liu HC, Wu X, Messing ME, Wallenberg LR, et al. High-resolution fluorescence diffuse optical tomography developed with nonlinear upconverting nanoparticles. ACS Nano. 2012;6(6):4788–95. doi:10.1021/nn3015807.
123. Chen GY, Ohulchanskyy TY, Kachynski A, Agren H, Prasad PN. Intense visible and near-infrared upconversion photoluminescence in colloidal $LiYF_4$:Er^{3+} nanocrystals under excitation at 1490 nm. ACS Nano. 2011;5(6):4981–6. doi:10.1021/nn201083j.
124. Liu Q, Sun Y, Yang TS, Feng W, Li CG, Li FY. Sub-10 nm hexagonal lanthanide-doped $NaLuF_4$ upconversion nanocrystals for sensitive bioimaging in vivo. J Am Chem Soc. 2011;133(43):17122–5. doi:10.1021/ja207078s.
125. Yang JP, Shen DK, Li XM, Li W, Fang Y, Wei Y, et al. One-step hydrothermal synthesis of carboxyl-functionalized upconversion phosphors for bioapplications. Chem Eur J. 2012;18(43):13642–50. doi:10.1002/chem.201202336.
126. Pokhrel M, Ak G, Sardar DK. High upconversion quantum yield at low pump threshold in Er^{3+}/Yb^{3+} doped La_2O_2S phosphor. Mater Lett. 2013;99:86–9. doi:10.1016/j.matlet.2013.02.062.
127. Pokhrel M, Kumar GA, Sardar DK. Highly efficient NIR to NIR and VIS upconversion in Er^{3+} and Yb^{3+} doped in M_2O_2S (M = Gd, La, Y). J Mater Chem A. 2013;1(38):11595–606. doi:10.1039/c3ta12205k.
128. Huang P, Zheng W, Zhou SY, Tu DT, Chen Z, Zhu HM, et al. Lanthanide-doped $LiLuF_4$ upconversion nanoprobes for the detection of disease biomarkers. Angew Chem Int Ed. 2014;53(5):1252–7. doi:10.1002/anie.201309503.
129. Resch-Genger U, Bremser W, Pfeifer D, Spieles M, Hoffmann A, DeRose PC, et al. State-of-the art comparability of corrected emission spectra.1. Spectral correction with physical transfer standards and spectral fluorescence standards by expert laboratories. Anal Chem. 2012;84(9):3889–98. doi:10.1021/ac2034503.
130. Villa I, Vedda A, Cantarelli IX, Pedroni M, Piccinelli F, Bettinelli M, et al. 1.3 μm emitting SrF_2:Nd^{3+} nanoparticles for high contrast in vivo imaging in the second biological window. Nano Res. 2015;8(2):649–65. doi:10.1007/s12274-014-0549-1.
131. Naczynski DJ, Tan MC, Zevon M, Wall B, Kohl J, Kulesa A, et al. Rare-earth-doped biological composites as in vivo shortwave infrared reporters. Nat Commun. 2013;4:2199. doi:10.1038/ncomms3199.
132. Hong G, Diao S, Chang J, Antaris AL, Chen C, Zhang B, et al. Through-skull fluorescence imaging of the brain in a new near-infrared window. Nat Photon. 2014;8(9):723–30. doi:10.1038/nphoton.2014.166.
133. Dang X, Gu L, Qi J, Correa S, Zhang G, Belcher AM, et al. Layer-by-layer assembled fluorescent probes in the second near-infrared window for systemic delivery and detection of ovarian cancer. Proc Natl Acad Sci U S A. 2016;113(19):5179–84. doi:10.1073/pnas.1521175113.
134. Hemmer E, Benayas A, Legare F, Vetrone F. Exploiting the biological windows: current perspectives on fluorescent bioprobes emitting above 1000 nm. Nanoscale Horiz. 2016;1(3):168–84. doi:10.1039/C5NH00073D.
135. Kim D, Lee N, Park YI, Hyeon T. Recent advances in inorganic nanoparticle-based NIR luminescence imaging: semiconductor nanoparticles and lanthanide nanoparticles. Bioconjugate Chem. 2017;28(1):115–23. doi:10.1021/acs.bioconjchem.6b00654.
136. Liu T-M, Conde J, Lipiński T, Bednarkiewicz A, Huang C-C. Smart NIR linear and nonlinear optical nanomaterials for cancer theranostics: prospects in photomedicine. Progr Mater Sci. 2017;88:89–135. doi:10.1016/j.pmatsci.2017.03.004.
137. Shao W, Chen G, Kuzmin A, Kutscher HL, Pliss A, Ohulchanskyy TY, et al. Tunable narrow band emissions from dye-sensitized core/shell/shell nanocrystals in the second near-infrared biological window. J Am Chem Soc. 2016;138(50):16192–5. doi:10.1021/jacs.6b08973.
138. Hatami S, Wurth C, Kaiser M, Leubner S, Gabriel S, Bahrig L, et al. Absolute photoluminescence quantum yields of IR26 and IR-emissive $Cd_{1-x}Hg_xTe$ and PbS quantum dots - method- and material-inherent challenges. Nanoscale. 2015;7(1):133–43. doi:10.1039/c4nr04608k.
139. Sapsford KE, Tyner KM, Dair BJ, Deschamps JR, Medintz IL. Analyzing nanomaterial bioconjugates: a review of current and emerging purification and characterization techniques. Anal Chem. 2011;83(12):4453–88. doi:10.1021/ac200853a.
140. Chan EM. Combinatorial approaches for developing upconverting nanomaterials: high-throughput screening, modeling, and applications. Chem Soc Rev. 2015;44(6):1653–79. doi:10.1039/c4cs00205a.